LATE QUATERNARY CARBONATE DEPOSITION AND OCEANOGRAPHIC PROCESSES IN THE SOUTHEAST ATLANTIC OCEAN

A Thesis

by

KATHERINE NICOLE CRABILL

Submitted to the Office of Graduate and Professional Studies of
Texas A&M University
in partial fulfillment of the requirements for the degree of

MASTER OF SCIENCE

Chair of Committee,	Niall Slowey
Committee Members,	Deborah Thomas
	Mitchell Lyle
Head of Department,	Shari Yvon-Lewis

May 2017

Major Subject: Oceanography

ABSTRACT

In the modern ocean, important water masses originating in the North Atlantic Ocean and Southern Ocean intersect the Namibian margin of southwest Africa at various water depths: Antarctic Intermediate Water (AAIW) occurs from 500 to 800 m, Upper Circumpolar Deep Water (UCDW) occurs from 800 to 1400 m, North Atlantic Deep Water (NADW) occurs from 1400 to 3800 m, and southern-sourced bottom water fills the remaining basin up to 3800 m water depth. Changes in the depth distributions and properties of these water masses through time are reflected by variations in the nature of the sediments accumulating along this margin. To investigate these variations, we examined a suite of sediment cores collected from water depths ranging from 550 to 3700 meters. Oxygen isotope and radiocarbon data indicate these cores have records corresponding to the past ~165 kyr, which corresponds to the two most recent glacial-interglacial cycles (MIS 1 through MIS 6). Discrete measurements of $CaCO_3$ content, X-ray fluorescence Fe/Ca ratios, and sediment density were made at regular intervals in the cores, and used to determine downcore profiles of $CaCO_3$ content and the mass accumulation rates (MAR) of total sediment, and the $CaCO_3$ and non-$CaCO_3$ components of the sediment. $CaCO_3$ content varies with glacial and interglacial stages such that lowest $CaCO_3$ contents occur during glacial MIS 2, 4 and 6, and the highest $CaCO_3$ contents occur during interglacial MIS 1 and 5. Temporal variations in MAR_{total}, MAR_{CaCO3} and $MAR_{non\text{-}CaCO3}$ indicate that these differences are primarily due to greater input of non-$CaCO_3$ sediment during glacial periods, rather than dissolution of $CaCO_3$

on the seafloor or decreased primary productivity at the sea surface. Comparison of the depth distributions of $CaCO_3$ content and MAR_{CaCO3} corresponding to the present time and the last glacial maximum (MIS 2) suggest that during MIS 2 the central depths of AAIW/UCDW and NADW were about 750 m and 2000 m, respectively, and southern-sourced bottom water occurred at depths below 3100 m. The relative abundances and MAR of quartz (indicated by X-ray diffraction) is greater during glacial stages than interglacial stages, because southwest Africa was more arid and offshore winds were stronger during glacial times.

ACKNOWLEDGEMENTS

I would like to thank my committee chair, Dr. Niall Slowey, and my committee members, Drs. Deborah Thomas and Mitchell Lyle, for their guidance and support throughout the course of this research.

Much of my sampling and all of my XRF work was completed at IODP, special thanks go to Phil Rumford and David Houpt at IODP for all of their help and kindness as I completed my research. Their assistance with the XRF scanning and core sampling was invaluable. Key guidance for my research came from our colleagues at the Scripps Institute of Oceanography, Dr. Chris Charles and Alan Foreman.

I want to thank my Oceanography family, for keeping me grounded and always there to support me. Thanks to my family for their unwavering support throughout my studies. Finally, thanks to my wonderful husband, Clint Crabill, for believing in me and pushing me to succeed. I could not have done this without all of your support, love and patience.

CONTRIBUTORS AND FUNDING SOURCES

Contributors

This work was supervised by a thesis committee consisting of committee chair, Dr. Niall Slowey of the Department of Oceanography, and my committee members, Drs. Deborah Thomas and Mitchell Lyle of the Departments of Geology and Oceanography, respectively. Dr. Christopher Charles and Mr. Alan Foreman of the Scripps Institution of Oceanography of the University of California are collaborators in this research. They provided the radiocarbon dates and foraminiferal oxygen isotope data. All other work conducted for the thesis was completed by the student independently.

Funding Sources

This work made possible by NSF grants OCE-0222101, OCE-1131224, and OCE-1131778. Additional fellowship support was provided by NSF grant DUE-1355807, as well as the Louis & Elizabeth Scherck and the Webber endowed fellowships via the Department of Oceanography. Teaching Assistantships and other support were provided by the Department of Oceanography.

TABLE OF CONTENTS

LIST OF FIGURES

LIST OF TABLES

1. INTRODUCTION

Significant variations in global ocean circulation and carbon cycling have occurred in conjunction with the glacial-interglacial climate cycles that punctuate the late Quaternary. As shown in Figure 1, glacial-interglacial changes in ocean circulation caused a reorganization of water masses in the South and North Atlantic Oceans (e.g. Duplessy et al., 1988; Curry and Oppo, 2005). Ice cores show significant fluctuations of atmospheric CO_2 occurred as well (e.g., Petit et al., 1999), and associated changes in the ocean chemistry have been measured (e.g. Broecker and Peng, 1982; Yu et al., 2016). In conjunction with these variations of environmental conditions, there were shifts of biological productivity in the oceans (e.g. Zahn et al., 1987; Freeman et al., 2016) and the influx of sediments to the ocean margins via rivers and winds (e.g. Rea, 1994; Nelson et al., 1986). The rates at which calcium carbonate ($CaCO_3$) rich sediments accumulate on the seafloor are intimately coupled to these processes (e.g. Archer and Maier-Reimer, 1994). Therefore, knowledge of the $CaCO_3$ sediment mass accumulation rates (MAR) will lead to a better understanding of the late Quaternary evolution of marine environmental conditions.

The rate that $CaCO_3$ sediment accumulates at a site on the seafloor may be influenced by several factors: (1) the influx of biologically produced $CaCO_3$ (e.g. Milliman, 1993); (2) dilution of $CaCO_3$ by terrigenous and siliceous sediments, which lowers the relative abundance of percentage by weight (e.g. Diester-Haass et al., 1988;

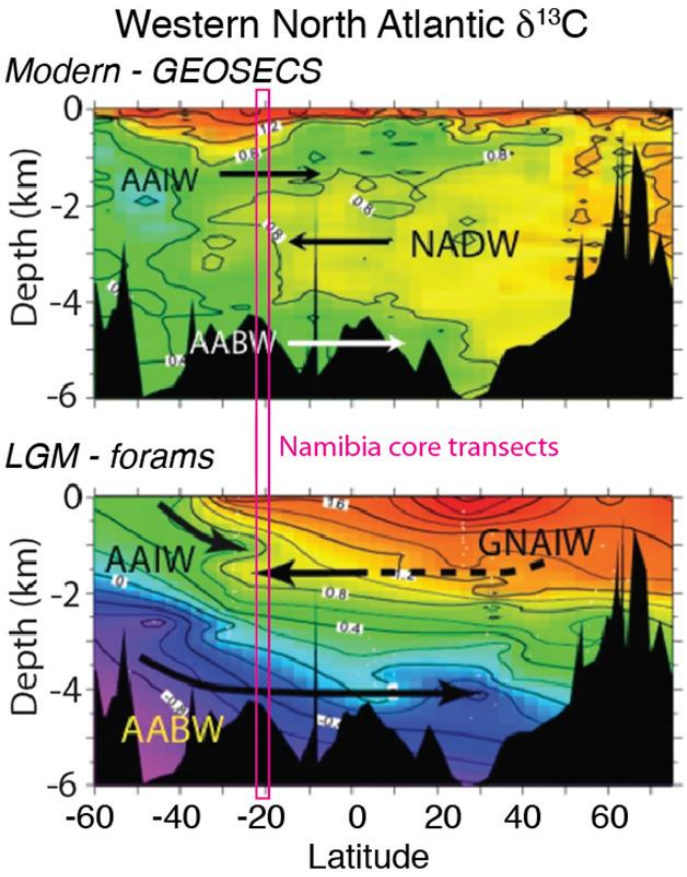

Figure 1. General patterns of water mass circulation. Modified from Curry and Oppo's (2005) illustration of the general patterns of water mass circulation now and during the last glacial maximum (LGM). Curry and Oppo's (2005) focused in the western Atlantic Ocean and was inferred from distributions of $\delta^{13}C$ of ΣCO_2. The patterns in the South Atlantic during the LGM differ from those that exist now: the core of northern source waters is shallow (~1500 m) and it penetrates as far as 30°S. Deep southern source water can be observed as far as 50°N, and shallow, southern source water appears to penetrate to at least 10°N, but there are too few data at intermediate water depths between about 25°S and 25°N in the western Atlantic to constrain its northward extent and interaction with northern source waters.

Curry and Lohmann, 1986); (3) dissolution of $CaCO_3$ at the seafloor due to the effects of temperature, pressure, and the concentration of CO_3^{2-} on the saturation state of ambient seawater with respect to $CaCO_3$ minerals (e.g., Balsam and McCoy 1987; Le and Shackleton, 1992; Bickert and Wefer, 1996) and the effect of organic matter degredation on saturation state of sediment porewaters (e.g., Emerson and Archer, 1990). As climate and ocean circulation change during glacial-interglacial cycles, the production of $CaCO_3$ within the water column and the accumulation of $CaCO_3$ on the seafloor may shift (e.g. Berger 1973; Crowley, 1985; Bickert and Wefer, 1996). In the North Atlantic, variable dilution by terrigenous sediments caused changes in the concentrations of $CaCO_3$ during the last glacial-interglacial cycle (Bacon, 1984; Keigwin and Jones, 1994). Studies generally suggest that dissolution is greater in the Atlantic and Southern Oceans during glacial periods (e.g. Balsam and McCoy, 1987), while greater preservation occurs in the Pacific Ocean during glacial periods (e.g. Hays, 1969; Farrell and Prell, 1989). These glacial-interglacial fluctuations of $CaCO_3$ storage and dissolution may reflect changes in the properties and geometries of individual water masses (e.g. Bickert and Wefer, 1996; Anderson and Archer, 2002).

Further efforts to understand how ocean circulation and carbon cycling have changed in conjunction with glacial-interglacial cycles are necessary. As shown in Figure 1 (Curry and Oppo, 2005), there is a limited amount of paleo-proxy information available to constrain how northern and southern sourced intermediate and deep water masses interacted in the crucial South Atlantic Ocean region during the late Quaternary. Most principal intermediate and deep water masses in the Atlantic Ocean intersect the

southwestern margin of Africa (Shannon, 1985), so sediments accumulating along this margin are ideally situated to monitor water mass interactions and their evolution over time. We aim to refine glacial boundaries of northern and southern sourced water masses by use of the $CaCO_3$ content and mass accumulation rates.

We collected a suite of cores of late Quaternary marine sediments from a range of water depths along the southwestern margin of Africa (Figure 2) that correspond directly to modern water masses (Figure 3). We used these cores to reconstruct how the concentrations and accumulation rates of $CaCO_3$ and other sediment constituents varied over the last two glacial-interglacial cycles. The relationships between these variations and changes in ocean circulation as well as the influxes of $CaCO_3$ and non-$CaCO_3$ sediments have been considered.

2. OCEANOGRAPHIC SETTING

We focused our efforts on the margin of Southwest Africa in a latitude band from 19.7 to 24.5°S, just south of the Walvis Ridge. The Walvis Ridge is an aseismic ridge that extends more than 2,000 km from the Mid-Atlantic Ridge to the African coast (Shaffer, 1984). Sediments accumulating on the continental shelf and slope at this site are derived from several principal sources. The overlying surface ocean waters are highly productive due to presence of the nutrient-rich Benguela Upwelling System, which is comprised of the northward flowing Benguela Current and eddies derived from it (Bremner, 1981; Shannon, 1985). Thus, there is a significant flux of biologically produced $CaCO_3$ and some biogenic silica to the seafloor (Bremner, 1981). Atmospheric high pressure systems established on a seasonal basis over the continent of Africa can create strong winds that transport large quantities of sand and dust out to sea; in our location this sediment can travel distances of 150 to 1500 km (Diester-Haass et al., 1988; Giresse, 2008; Shannon, 1985). There is not a significant influx of sediments to the study area from local rivers (Milliman and Farnsworth, 2013). The main source of riverine sediments to the overall region is the Orange River, which is over 1,000 km to the south, so only fine muds may make it to the study site (Diester-Haass et al.,1988; Giresse, 2008; Milliman and Farnsworth, 2013). Transport of sediments along the seafloor due to the large upwelling system in the region could preferentially sort sediments, such that coarser grains accumulate primarily on the shelf and upper slope, and finer grains are transported further offshore (Huhn et al 2007).

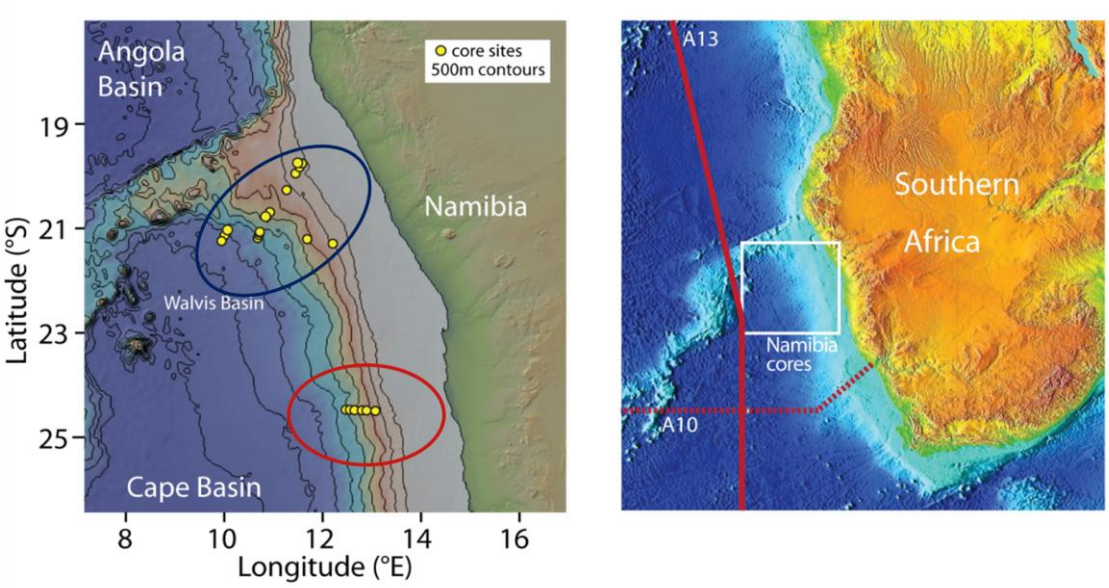

Figure 2. Left: Bathymetry of the southwest margin of Africa and Walvis Ridge. The locations of cores being used for this study show by yellow circles. Walvis Ridge transects with cores used are located in (blue) oval, Cape Basin transect with cores used are located to the south, in the (red) oval. Right: Red lines indicate WOCE transects A10 dashed line and A13 solid line near sampling region.

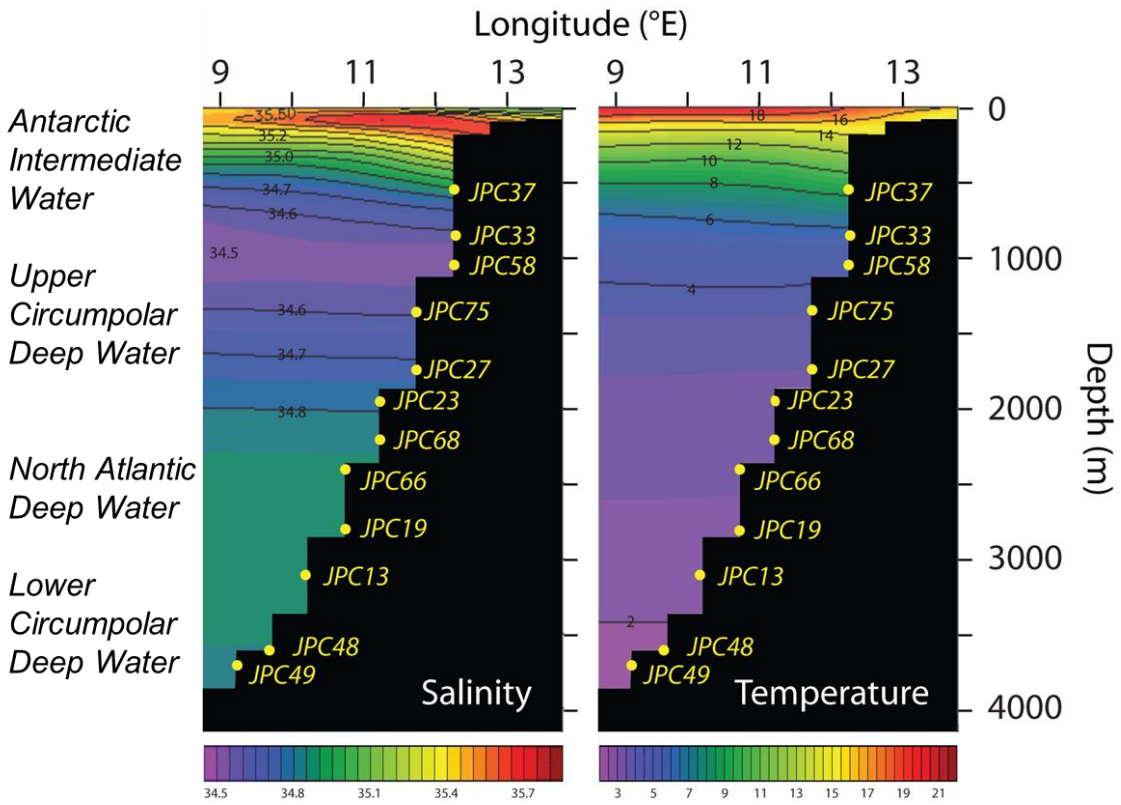

Figure 3. Properties of modern ocean waters that intersect the Namibian margin. A transect along 22.3°S from SODAsi.3 (B. Giese, personal communication, May 5, 2016), along with relative stacking of water masses was used. The yellow circles show the locations of cores being used for this study.

Along this portion of the margin of Africa, there is a confluence of water masses that originate from the North Atlantic and Southern Oceans (Figure 3). The identities and vertical sequence of the modern water masses in the Walvis Ridge and Cape Basin region can be inferred from the temperature, salinity, and other properties of seawater measured on nearby WOCE Lines A10 and A13 (Figure 2): Antarctic Intermediate Water (AAIW) and Upper Circumpolar Deep Water, flow northward at depths of 500 to 1400 m and 800 to 1400 m, respectively, while North Atlantic Deep Water (NADW) flows southward at 1400 to 3800 m. All three water masses flow over the Walvis Ridge and intersect the sediment margin along Namibia. Below this is the Lower Circumpolar Deep Water (LCDW) that flows northward and fills the bottom of the Cape Basin to the south below 3800 m, making it north of the Walvis Ridge in only the deepest valleys in select locations along the Ridge (Huneke and Henrich, 2011; Koltermann et al., 2011). Table 1 lists the characteristics and depth ranges of the intermediate and deep water masses in the study area (Emery and Meincke, 1986; Koltermann et al., 2011).

This layering of water masses with their inherent characteristics, together with the effect of increasing pressure with depth, determines the saturation state of the waters with respect to calcium carbonate minerals. The saturation states of aragonite and calcite in seawater, $\Omega_{mineral}$, are determined by the product of the concentrations of dissolved calcium and carbonate ions in seawater divided by the mineral's solubility product, K_{sp}, such that $\Omega_{mineral} = ([Ca^{2+}] * [CO_3^{2-}])/K_{sp}$. When $\Omega_{mineral} = 1$ the saturation state of seawater is at equilibrium with respect to the mineral; when $\Omega_{mineral} > 1$ the seawater is supersaturated with the mineral, and the mineral may precipitate; and when $\Omega_{mineral} < 1$

the seawater is under saturated with the mineral, and it will dissolve (Morse and MacKenzie, 1990; Millero, 2007). The carbonate mineral saturation states of water masses can affect the nature of seafloor sediments. In the modern ocean, the $\Omega_{mineral}$ values of water masses from the Southern Ocean are less than water masses from the North Atlantic, so the southern sourced waters tend to be more corrosive with respect to calcium carbonate sediments exposed at the seafloor (e.g. Reid, 1996).

As described by Curry and Oppo, (2005) the water mass patterns in the South Atlantic Ocean during the LGM differ from those that exist now: the core of northern sourced waters was shallower than today, ~1500 m and penetrates as far as 30°S. Deep southern sourced water can be observed as far as 50°N, and intermediate, southern source water appears to penetrate to at least 10°N. However, there are limited data at intermediate water depths between about 25°S and 25°N in the western Atlantic to constrain its northward extent and interaction with the northern source waters. We are investigating the glacial to modern evolution of the water masses as inferred from the aspects of the sediments in cores collected at 19-21°S along the eastern South Atlantic margin near Namibia.

Table 1. Temperature-salinity characteristics and relative water depth ranges. Intermediate and deep water masses present by comparing Emery, and Meincke, (1986) characteristics with WOCE and SODAsi.3 for this study area (Koltermann et al., 2011; B. Giese, personal communication, May 5, 2016).

Water layer	Water mass	Temperature °C	Salinity pss	Silicate µmol/kg	Oxygen µmol/kg	Density γ
Intermediate	Antarctic Intermediate Water (500-800 m)	2.0-6.0	≤34.40	43-46	>220	27.40
Deep	Upper Circumpolar Deep Water (800-1400 m)	4.0-3.0	34.35	50-55	<185	27.84
	North Atlantic Deep Water (1400-3800 m)	1.0-3.0	34.86	40-42	220-240	28.05
	Lower Circumpolar Deep Water (3800 m-bottom)	0.0-2.0	34.62-34.73	100-105	210-220	28.20

3. METHODS

The sediment cores used for this study (Table 2) are 10-cm diameter jumbo piston cores (JPC) and gravity cores (GC) collected during *R/V Melvill*e cruise MEL VAN 09 from two regions of the continental slope of Namibia, just south of the Walvis Ridge (Figure 3). These cores were taken 130 to 350 km offshore along transects located in a very narrow geographic region, so at any given time similar biological productivity is likely to have occurred in the surface waters above all core sites. The core sites span the water depth range of 567 to 3678 m, which corresponds to the depths of most of the principal intermediate and deep water masses in the modern South Atlantic Ocean (Figure 3). High-resolution chirp subbottom profiles of the seabed at the core sites displayed laterally continuous, parallel reflectors, consistent with hemipelagic drape (e.g., Damuth 1980).

When the cores were brought aboard the ship, they were cut into 1 or 1.5 m long sections and capped. After the sediments equilibrated with the laboratory temperature, their bulk densities were determined at a depth interval of 2 cm using a GeoTek multisensor core logger (MSCL) based upon Gamma ray attenuation. The core sections were subsequently stored under refrigerated conditions on the *R/V Melvill*e and at the Integrated Ocean Discovery Program core repository at Texas A&M University.

When the cores were brought aboard the ship, they were cut into 1 or 1.5 m long sections and capped. After the sediments equilibrated with the laboratory temperature, their bulk densities were determined at a depth interval of 2 cm using a GeoTek

Table 2. Sediment cores collected and sampled in this study. 10-cm diameter jumbo piston cores (JPC) and gravity cores (GC) collected during R/V Melville cruise MEL VAN 09 sampled for this study. Once $CaCO_3$ contents was determined, data from JPC41, JPC35, JPC29, GC28 and GC34 were excluded, the data obtained from these cores indicated sediments were disturbed by downslope processes and/or seafloor currents, indicated as the bolded core names.

Name	Latitude (°S)	Longitude (°E)	Water Depth (m)	Core Length (cm)
GC 12	21.182	10.637	3127	190.5
JPC 13	21.182	10.638	3092	1084.5
JPC 15	21.121	10.660	3023	1100
GC 18	21.080	10.675	3023	204.5
JPC 19	21.080	10.676	2816	727.5
GC 20	21.064	10.065	2705	189
JPC 21	21.064	10.682	2680	687.5
GC 22	20.798	10.808	1980	196
JPC 23	20.798	10.808	1977	928.5
GC 26	20.687	10.887	1803	201.4
JPC 27	20.687	10.887	1804	925.5
GC 28	20.263	11.227	1153	173
JPC 29	20.263	11.227	1163	1108
GC 32	19.947	11.408	843	147
JPC 33	19.947	11.408	851	1006.5
GC 34	19.825	11.490	678	183.5
JPC 35	19.825	11.490	680	1091
GC 36	19.754	11.543	565	184
JPC 37	19.755	11.543	567	1108.5
JPC 41	21.202	11.645	1603	887
JPC 48	21.128	9.966	3571	928.5
JPC 49	21.240	9.901	3678	949.5
GC 57	21.287	12.167	1031	175
JPC 58	21.287	12.167	1037	993.5
JPC 64	24.467	12.433	2646	813
JPC 66	24.470	12.517	2406	687.5
JPC 68	24.473	12.609	2203	730.5
JPC 72	24.479	12.759	1902	911.5
JPC 74	24.482	12.855	1704	884.5
JPC 75	24.489	13.034	1306	1124
JPC 89	19.765	11.447	701	1065.5

multisensor core logger (MSCL) based upon Gamma ray attenuation. The core sections were subsequently stored under refrigerated conditions on the *R/V Melvill*e and at the Integrated Ocean Discovery Program core repository at Texas A&M University.

At the repository, the core sections were split along their longitudinal axes and their sediments were inspected visually. The cores selected for this study did not exhibit sedimentary structures indicative of disturbance by debris or turbidity flows, and is a a regionally consistent lithologic stratigraphy. A total of 2,432 sediment samples for $CaCO_3$ content and mineralogy analyses were taken from 21 JPCs and 10 GCs. These samples were typically taken from the cores at a depth interval of 10 cm, though a few cores were sampled at depth intervals of 5 or 20 cm. Sediment samples were also taken at regular depth intervals for foraminiferal stable isotope and geochemical analyses by other members of our research team.

A 3rd Generation Avaatech X-ray fluorescence (XRF) scanner was used to measure downcore variations in the elemental composition of bulk sediment, the ratio of Fe/Ca peak areas was used to compare to the $CaCO_3$ content in the discrete samples (e.g. Jansen et al., 1998; Richter et al., 2006). The X-ray source was initially run at 10 kV and the detector count time was 20 seconds for each measurement, and measurements were taken at depth intervals that varied from 1 to 3 cm depending on the core. Later, a 9 kV source tube was used, but the detector remained the same. After changing the voltage tube, the same standard count time of 20 seconds was maintained, and a depth interval of 2 cm was used. JPC23 was rerun at the new settings to confirm data collected before and after the hardware change were comparable.

Samples taken for $CaCO_3$ content and mineralogy were dried for 24 hours at 50°C, then ground with an agate mortar and pestle and sieved to confirm sediment grains were 125 µm or less in size. To determine $CaCO_3$ content, approximately 15 mg of sediment from each sample was placed into a Vaccutainer vial and sealed with a rubber septum. Batches of 44 sample vials were loaded into the carousel of an AutoMate FX automatic preparation module attached to an UIC model CM-5012 CO_2 coulometer. The AutoMate uses needles to penetrate the septa and flush each vial with a continuous stream of nitrogen gas. It then introduces 10% phosphoric acid (H_3PO_4) that thoroughly wets the sample and reacts with sedimentary $CaCO_3$ to produce CO_2 gas, which is precisely measured by the coulometer. The amount of CO_2 is stoichiometrically related to the mass of $CaCO_3$ in the sample. The analytical precision of individual weight percent $CaCO_3$ measurements made during this study was ±0.44%, as indicated by the standard deviation of replicate measurements of the in-house Midway standard, which is homogenized marine sediment from W8709A-5BC (Piela, 2010).

The relative abundance of various $CaCO_3$ minerals within selected samples was determined based upon X-ray diffraction peak areas (Neumann, 1965; Milliman, 1973). Prepared sample material was loaded onto acrylic disks and then analyzed using a Buker D8 X-ray diffractometer system with a Cu filament X-ray tube over the range of 25-32° 2θ. This range of 2θ values includes primary and secondary diffraction peaks of aragonite, low-Mg calcite, high-Mg calcite, dolomite, gypsum, and quartz.

Variations in downcore profiles of foraminiferal and bulk sediment $\delta^{18}O$ values were used as the primary indicator of sediment ages. Profiles of benthic foraminiferal

Cibicidoides wuellerstorfi and planktonic foraminiferal *Globigerina bulloides* $\delta^{18}O$ values were generated by our colleagues at the Scripps Institute of Oceanography for cores JPC 21, JPC23 and JPC49, along with $\delta^{18}O$ values for specific depths in 12 other cores. To expand the isotope records to the shallower cores, bulk sediment $\delta^{18}O$ records were generated for cores JPC58 and JPC35 at the Texas A&M University. At both institutions, isotopic measurements were made using MAT 253 mass spectrometers with Kiel IV preparation systems following standard methods (e.g., Slowey & Curry, 1995; Ostermann & Curry, 2000). The analytical precision of individual $\delta^{18}O$ measurements made during this study was ±0.06‰, as indicated by the standard deviation of replicate measurements of the NBS-19 standard.

4. RESULTS AND DISCUSSION

4.1 Sediment Age and $CaCO_3$ Content Estimates

The ratios of stable isotopic compositions of foraminiferal $\delta^{18}O$ values were measured in several cores by our colleagues at SIO (Figure 4, top). The data spans the last 200,000 years, and the fluctuations in $\delta^{18}O$ are associated with the Marine Isotope Stages (MIS) as seen as glacial-interglacial cycles defined by Emiliani (1955) and Shackleton and Opdyke (1973). The more negative values correspond to interglacial periods, 1 and 5. The more positive values correlate to glacial periods, 2-4 and 6. The $\delta^{18}O$ values ranged from 2.5 to 4.7%. In the cores where bulk sediment $\delta^{18}O$ values were measured (Figure 4, bottom), the data spans 60,000 years. The $\delta^{18}O$ values range from 0.5 to 3‰ and are also associated with the glacial-interglacial cycles MIS 1-3. As shown in Figure 4, the downcore profiles of foraminiferal and bulk sediment $\delta^{18}O$ values indicate that the cores used in this study contain sediments that were deposited in a continuous fashion during the late Quaternary.

The uppermost sediments in all cores correspond to MIS 1, and the deeper portions of the cores are from MIS 2 to 7. As part of this overall project, preliminary foraminiferal radiocarbon dates were generated for several depths in the upper portions of some sediment cores (C. Charles and A. Foreman, personal communication, Nov. 30, 2015). While these dates were not incorporated directly into the age-depth models for the cores, they did provide valuable confirmation of the approximate location of the

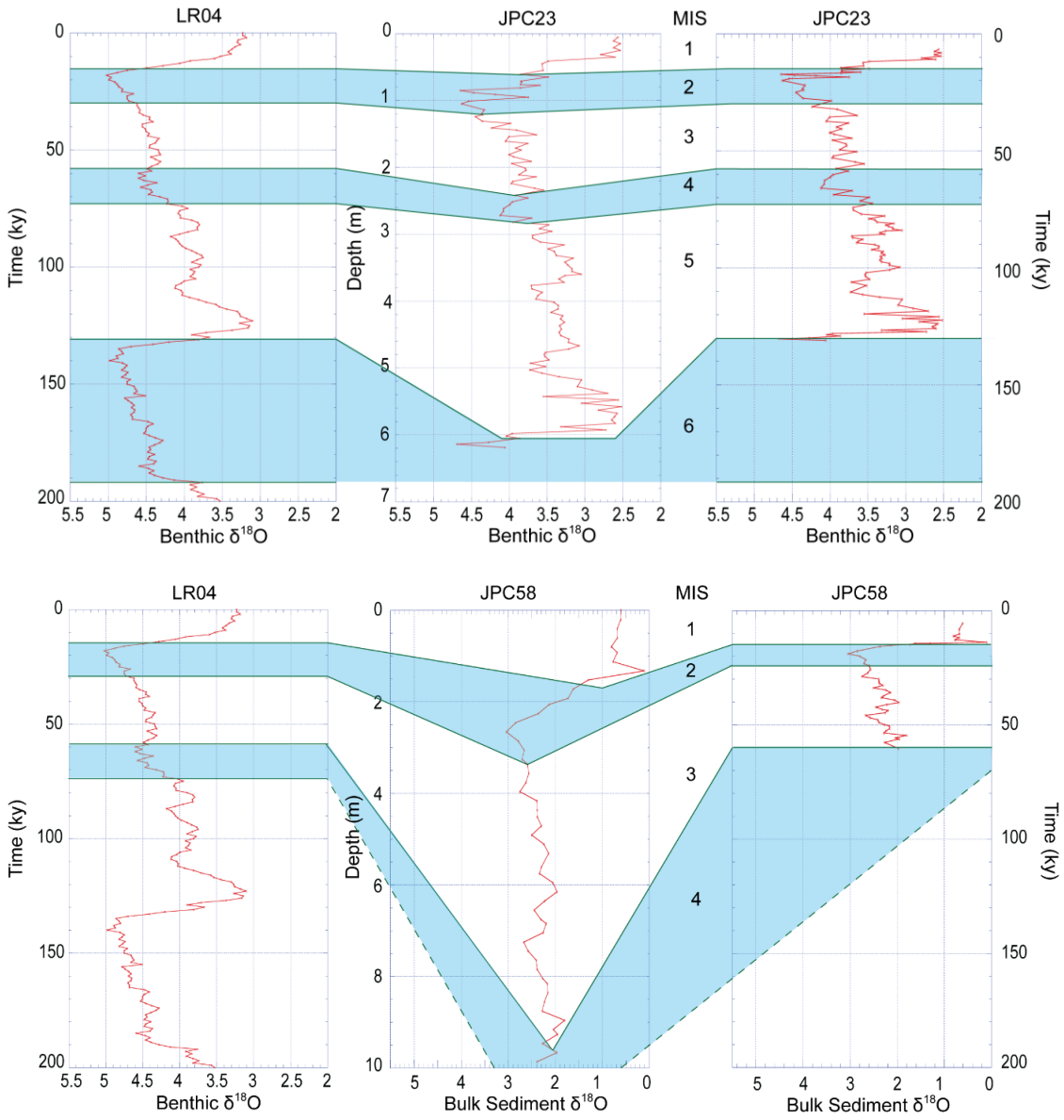

Figure 4. Top. Correlation of the marine oxygen isotope stages (MIS). Correlations between the benthic foraminiferal $\delta^{18}O$ records of Lisieki and Raymo (2004) and the Namibian margin core JPC23 were used (B. data from our collaborators at the Scripps Institute of Oceanography). Bottom. Correlation of the marine oxygen isotope (MIS) stages in the bulk sediment $\delta^{18}O$ records of Lisieki and Raymo (2004) were generated for an additional 2 cores JPC58 and JPC35 at the Texas A&M University, JPC35 not shown. Such correlations and radiocarbon dates are the basis of the age models for our Namibian cores.

boundary between sediments corresponding MIS stages 1 and 2 as determined from downcore variation in the foraminiferal and bulk sediment $\delta^{18}O$ values.

As shown in Figure 4, the $\delta^{18}O$ depth series in our sediment core records were correlated with the $\delta^{18}O$ time series in the LR04 Stack, which Lisieki and Raymo (2005) created from a globally distributed suite of foraminiferal $\delta^{18}O$ records that they placed on a common age model. The ages of several features in the $\delta^{18}O$ records were then associated with specific depths in our sediment cores (Table 3); the ages of intervening depths in our cores were estimated by linear interpolation.

Close correspondences exist between changes in the downcore profiles of $CaCO_3$ contents measured in discrete sediment samples and the Fe/Ca ratios measured by XRF, where the $CaCO_3$ content is inversely related to the Fe/Ca ratio (Figure 5). This inverse relation between the $CaCO_3$ content and Fe/Ca ratio could be due to several reasons[1], such as (1) more iron is in the terrigenous sediments compared to $CaCO_3$ sediments, (2) the Fe-oxide coating on fine sediments has a greater surface area, and those sediments had originated on land and/or due to variation of redox state of sediment porewaters (3) increased aeolian presence in the glacial periods transport greater amounts of terrigenous iron out into the ocean. Evidently the relative importance of these factors is not constant at all seafloor sites because the relationships between $CaCO_3$ contents and Fe/Ca ratios were not the same for all cores; rather, the relationships vary in a generally consistent fashion with water depth (Figure 6).

[1] Changes in sediment density/porosity do not cause variations in measurements of $CaCO_3$ content and Fe/Ca ratios.

Table 3. Age tie points in key sediment cores. The list of tie points in the three key cores where specific features in the $\delta^{18}O$ record are identified at depths within the cores and then associated to ages.

JPC21		JPC23		JPC49		JPC58	
Core Depth (m)	Age (ky)	Core Depth (m)	Age (ky)	Core Depth (m)	Age (ky)	Core Depth (m)	Age (ky)
0.01	2.00	0.02	6.32	0.06	2.78	0.04	3.47
0.21	7.87	0.56	13.94	0.35	8.83	0.52	9.79
1.09	17.81	1.01	19.2	0.37	9.34	1.43	14.39
1.11	18.31	1.16	22.42	0.55	14.43	1.73	14.42
2.936	66.00	1.231	24.61	0.83	19.00	2.36	15.98
3.646	84.00	1.371	29.83	1.13	22.73	2.48	18.00
3.896	88.00	1.511	34.91	1.15	23.65	2.86	20.00
4.176	95.00	1.531	35.56	1.19	25.76	3.89	29.00
4.626	109.00	2.031	47.59	1.27	29.90	9.41	57.00
5.026	121.00	2.648	63.65	1.56	35.46	9.77	61.56
5.176	126.00	2.708	65.66	1.58	35.92		
5.526	130.00	2.728	66.28	2.42	56.50		
		3.168	78.42	2.44	56.99		
		3.348	80.96	2.723	62.37		
		3.588	83.88	2.743	62.75		
		3.618	84.29	3.023	68.44		
		4.658	99.52	3.043	68.83		
		4.678	99.92	3.443	75.08		
		4.969	107.19	3.463	75.39		
		4.989	108.06	3.523	78.34		
		5.029	110.50	3.543	78.72		
		5.169	113.30	3.823	84.00		
		5.189	113.75	3.843	84.41		
		5.469	120.82	4.915	106.43		
		5.489	121.17	4.935	106.85		
				5.035	109.06		
				5.159	111.98		
				5.499	120.53		
				5.519	121.03		
				5.725	125.29		
				5.759	125.99		
				5.979	130.01		
				5.999	130.99		

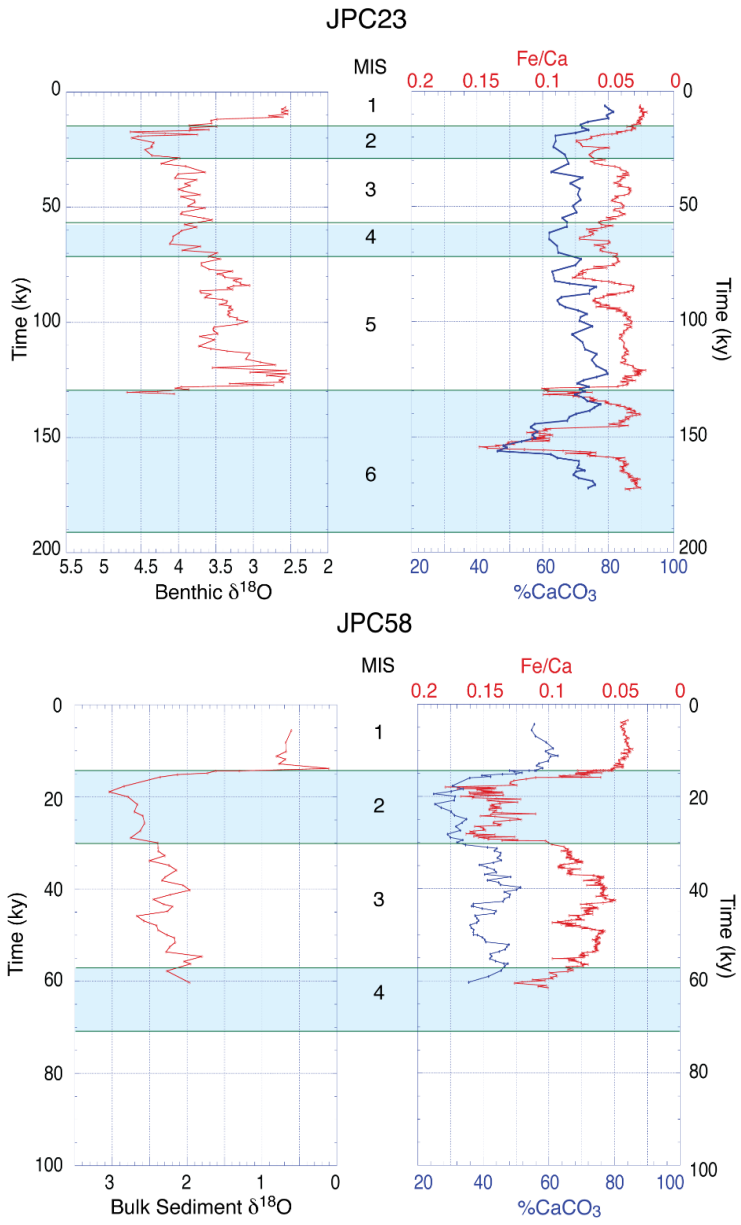

Figure 5. Top. Down-core profiles of benthic foraminiferal $\delta^{18}O$, weight $\%CaCO_3$, and the ratio of Fe/Ca XRF counts from core JPC23. These profiles exhibit coherent variations, and these variations coincide with shifts in glacial-interglacial climate with lower $\%CaCO_3$ occurring during periods of colder climate and lower sea level. The values of $\%CaCO_3$, and Fe/Ca counts are inversely related (note: values on the Fe/Ca axis are plotted such that values decrease left to right). Bottom. Down-core profiles of bulk sediment $\delta^{18}O$, weight $\%CaCO_3$, and the ratio of Fe/Ca XRF counts from core JPC58 exhibit the same coherent variations as the benthic foraminiferal $\delta^{18}O$ as seen above.

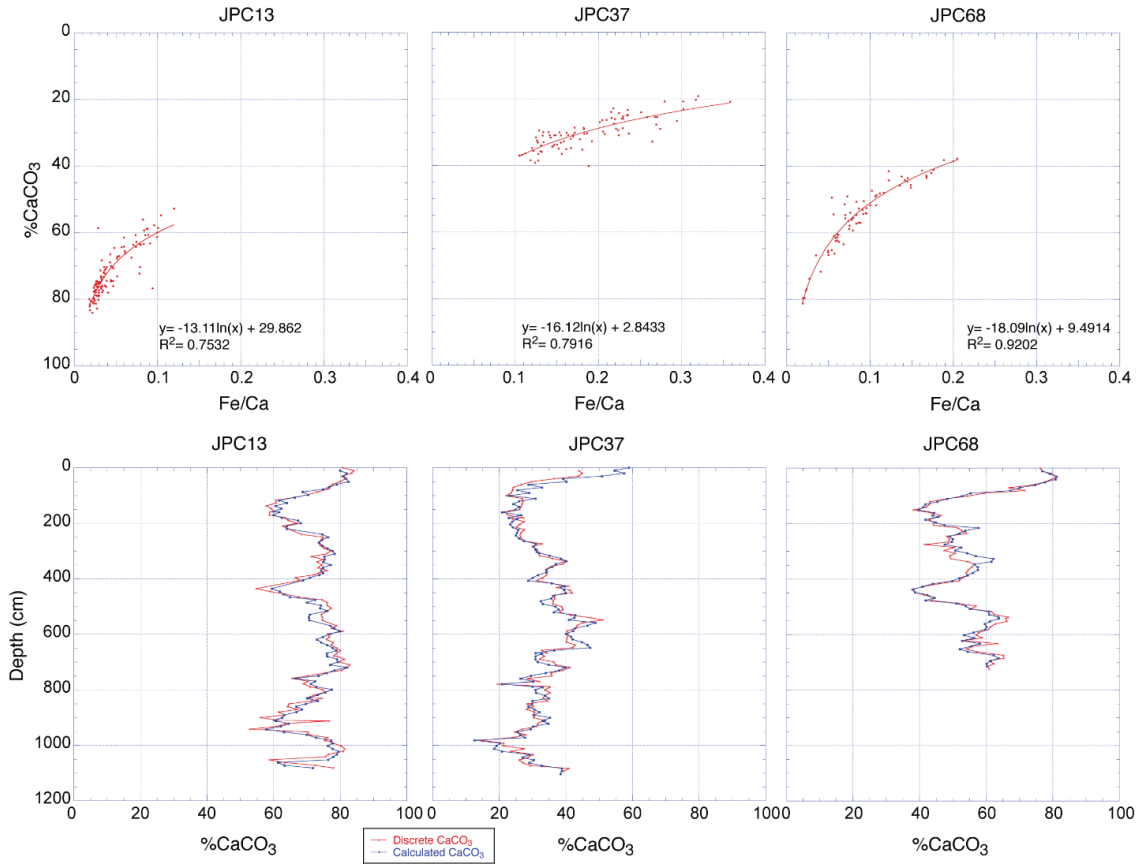

Figure 6. Top. The strong correlation between $\%CaCO_3$ and Fe/Ca from the XRF. The R^2 values are shown for each core in the plotted space. Bottom. The discrete $CaCO_3$ measurements (red) and the calculated $CaCO_3$ (blue) show the strong correlation.

For each core, an equation of the general form $y = a * \ln(x) + b$ was fitted to the pairs of Fe/Ca and $CaCO_3$ values measured at the same depths in the core and a coefficient of determination (R^2) was calculated as a measure of the goodness of fit of the equation to the data (Figure 6).

The fitted equations were the basis for using the XRF data to generate robust estimates of $CaCO_3$ content every 2 cm depth in the cores. The reasonableness of this approach was checked by comparing the $CaCO_3$ contents measured from discrete samples and the $CaCO_3$ contents estimated from Fe/Ca values – the standard deviation of the differences between values determined these two ways was within ±2.5% for each core (Figure 6). Thus, it was possible to generate $CaCO_3$ content records of higher spatial/temporal resolution than would otherwise be feasible.

The cores used in this study displayed very similar downcore variations of $CaCO_3$ content, and the patterns of $CaCO_3$ content change were consistently related to the glacial-interglacial stages (Figure 7). Therefore, once $\delta^{18}O$ based age-depth models were established for cores with sufficient $\delta^{18}O$ data, age-depth models for the remaining cores were determined by correlating the profiles of $CaCO_3$ content among all of the cores (Figure 7). There were a few cores in this study that were excluded from further study due to missing upper sediment within the core or downslope transport that may have played a role as seen in the $CaCO_3$ contents and or bulk sediment $\delta^{18}O$ (JPC29, JPC35, JPC41 and corresponding GCs: GC28 and GC34).

When plotting sediment core information as a function of water depth, we

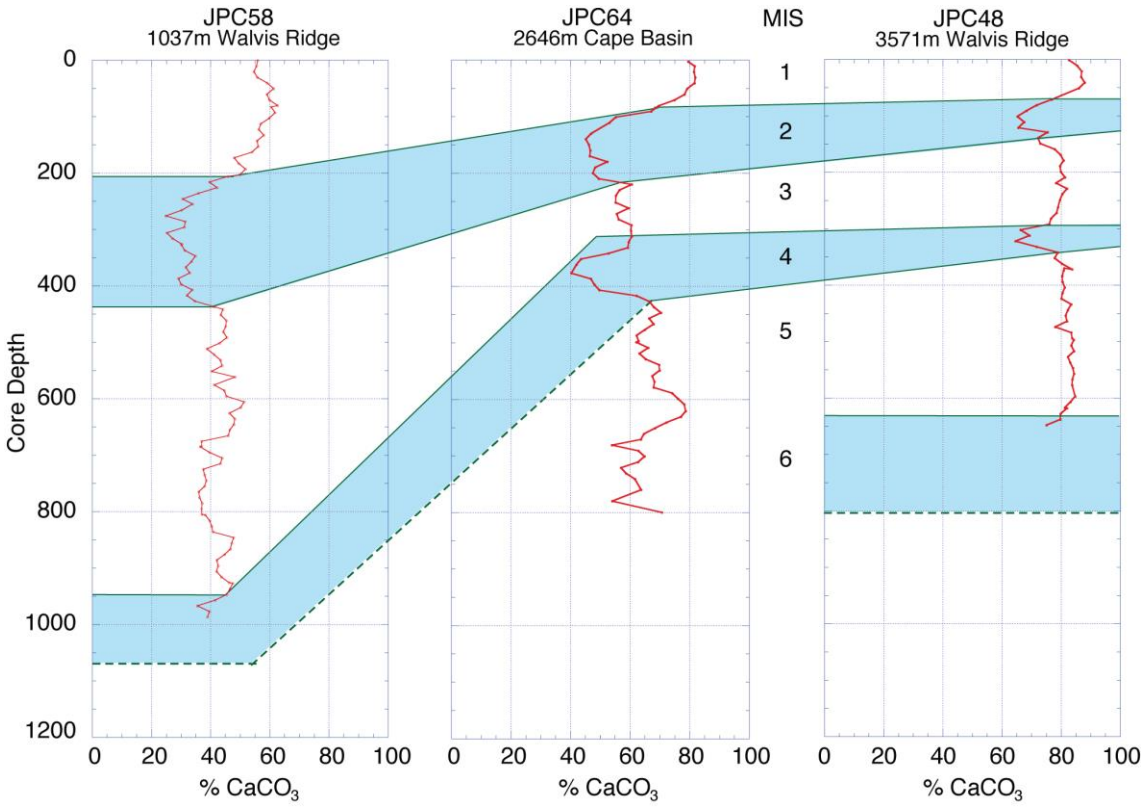

Figure 7. Examples of down-core variations of carbonate content associated with MIS. The carbonate content measured in Namibian cores from different water depths/water masses. Similar patterns of variability occur in each core (correlative relative minima indicated in blue shading).

Table 4. Average sea level for each MIS. Adapted from Waelbroeck et al., 2002.

MIS	Mean Sea Level (m)
1	0
2	-120
3	-71
4	-67
5	-26
6	-88

accounted for temporal variations of sea level based upon the differences between modern sea level and the sea level that existed during the MIS's. Table 4 shows values for the mean sea level during each MIS's we calculated from the sea-level history of Waelbroeck et al. (2002).

4.2 Sediment $CaCO_3$ Contents and the $CaCO_3$ Saturation State of Seawater

At the Walvis Ridge and Cape Basin locations the $CaCO_3$ content fluctuates as much as 40% in a single sediment core, and the total $CaCO_3$ content in all cores ranges from 15 to 88%. Cape Basin cores average a lower measured $CaCO_3$ contents ranging from 36 to 62% compared to the Walvis Ridge cores with an average measured range of 33 to 79% (Figure 8).

During sampling, the cores at water depths >3000 m were observed to be very fine grained and almost completely white in color. Although the $CaCO_3$ content in these cores is high, qualitative inspection suggested some breakdown and dissolution of $CaCO_3$ sediment grains. Broecker and Broecker (1974) showed significant amounts of $CaCO_3$ dissolution can occur and yet it may not be clearly evident in measured $CaCO_3$ content. To provide a context for consideration of possible dissolution of $CaCO_3$, the saturation state of seawater in this region was calculated using the CO2sys program (Pierrot and Wallace, 2006) and WOCE transect data for alkalinity. The saturation state for aragonite and calcite are defined by $\Omega_{\text{arag or calcite}} = 1$, in this region there are two water depths, 450 m and 2500 m, where Ω_{arag} falls below 1 becoming undersaturated, Ω_{calcite} decreases below 1 at one water depth, 4000 m (Figure 9).

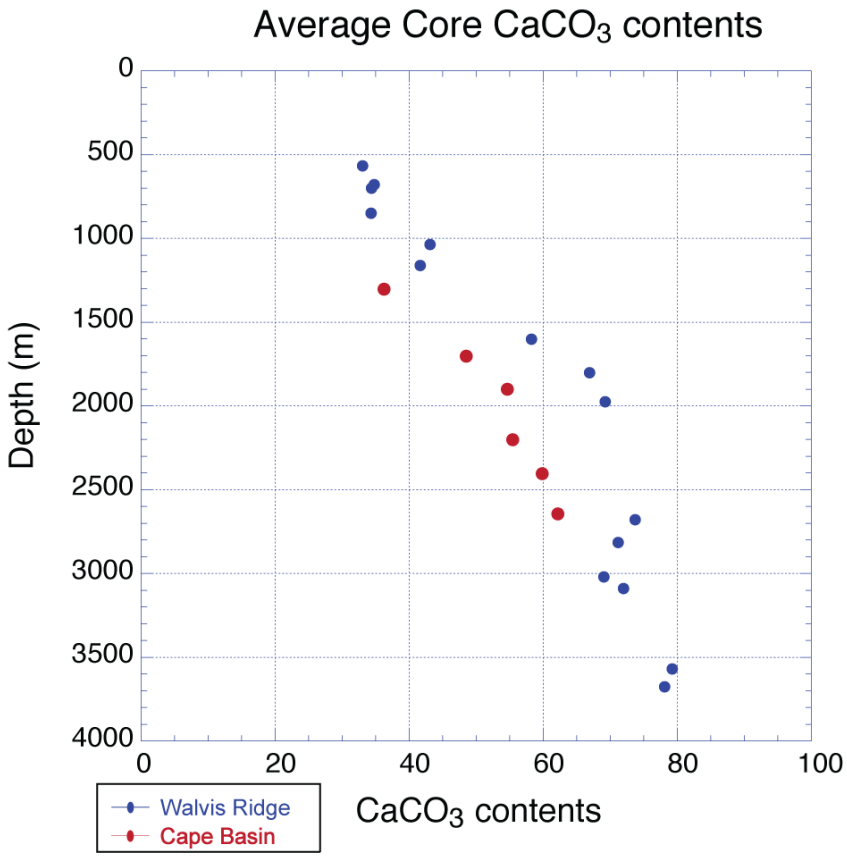

Figure 8. Average core $CaCO_3$ contents for Walvis Ridge and Cape Basin at every water depth.

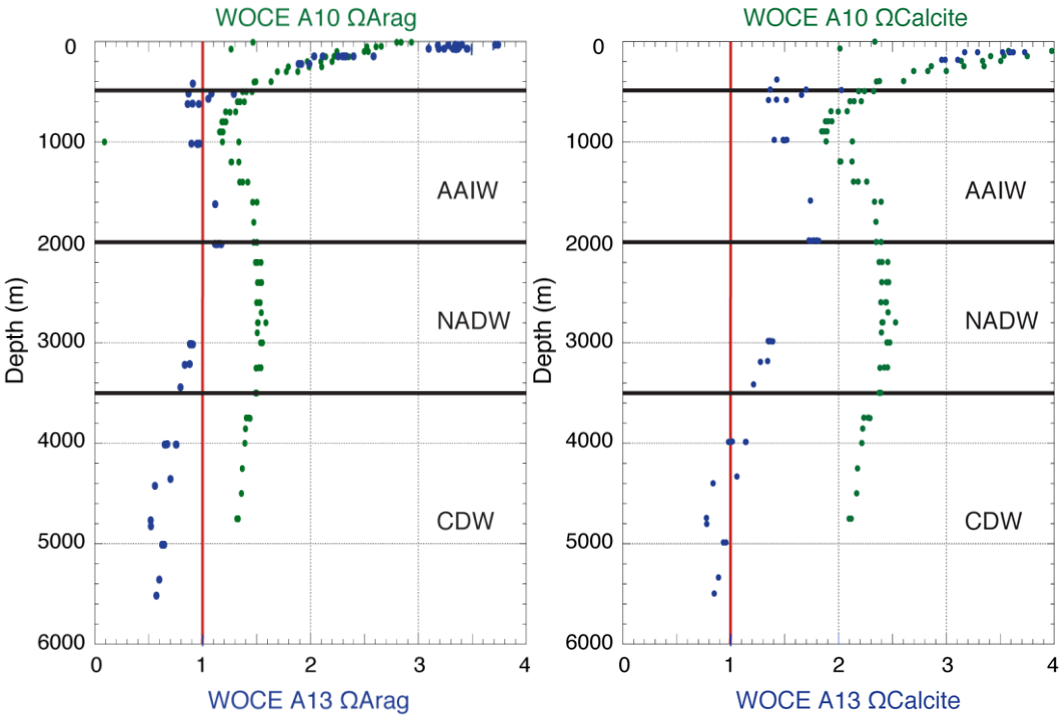

Figure 9. Aragonite saturation state. Left. Aragonite saturation state (Ω) of the water column calculated with CO2sys from WOCE A10 and A13 transects of stations nearest to our study site. Water mass depths have been overlaid. Right. Calcite saturation state of the water column calculated with CO2sys from WOCE A10 and A13 transects nearest our study site (Pierrot and Wallace, 2006; Koltermann et al., 2011).

Given these profiles, one might expect dissolution at deeper seafloor sites to result in lower $CaCO_3$ contents, rather than the higher $CaCO_3$ contents actually observed. Why does this apparent paradox exist? What are the relationships between temporal and spatial variations of oceanographic conditions and sedimentary processes? We followed a stepwise approach to address these questions.

4.3 $CaCO_3$ Contents of Late Holocene and Last Glacial Maximum Seafloor Sediments

The late Holocene-aged sediments (0-5 ka) were identified within each core and their mean $CaCO_3$ contents were calculated. As shown in Figure 10, as the water depth increases from about 550 m to 3650 m there is an overall increase in mean late Holocene sedimentary $CaCO_3$ content from about 50 to 85%. Only sediments in cores JPC64 and JPC66 deviate in a noticeable way from this overall pattern – their late Holocene $CaCO_3$ contents (41 and 46%) are only about one half of those in other cores from similar water depths. These two cores are from the Cape Basin region, whereas, all but one other core are from the Walvis Ridge region. Water properties in the two regions are similar, so this difference in $CaCO_3$ content likely reflects a regional difference in the relative inputs of $CaCO_3$ and non-$CaCO_3$ particles.

The patterns by which variations of $CaCO_3$ content occur with water depth presumably reflect variations in modern environmental conditions. $CaCO_3$ content increases from about 50 to 60% over the water depth range of about 550 to 1600 m (1% per 100 m), $CaCO_3$ content increases from about 60 to 80% over the water depth range of 1600 to 2000 m (5% per 100 m), and $CaCO_3$ content increases from about 80 to 85%

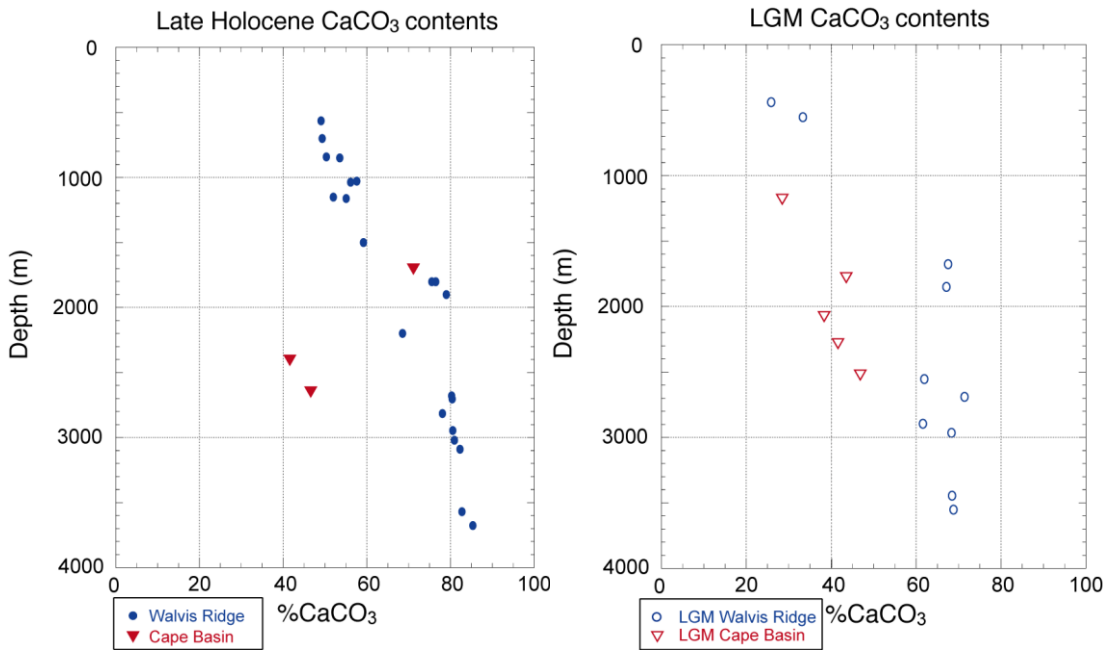

Figure 10. Late Holocene (0-5 ky age) $CaCO_3$ content versus water depth. Filled circles (blue) indicate Walvis Ridge region cores; filled triangles (red) indicate Cape Basin region cores. LGM $CaCO_3$ content, Walvis Ridge cores open circles (blue), Cape Basin cores open triangles (red).

over the water depth range of about 2000 to 3650 m (0.3% per 100 m). Thus, $CaCO_3$ content increases over all water depth intervals. Why does $CaCO_3$ content increase from about 50 to 60% over the water depth range of about 550 to 1600 m while there is a decrease in the saturation state of seawater with respect to $CaCO_3$ minerals? If the rate of $CaCO_3$ mineral production in the surface ocean waters above all core sites is similar, several possible explanations for the change in sedimentary $CaCO_3$ content exist: (1) There may be lower fluxes of terrigenous sediments and/or biogenic silica to the seafloor at deeper water depth core sites because the sites are farther from the continent and the thicker overlying water column allows for more dissolution of biogenic silica in the seawater. (2) There may be lower fluxes of organic matter to the seafloor at deeper water depth core sites because the thicker overlying water column allows for more degradation of organic matter in the seawater, so less degradation occurs at the seafloor and, hence, there is less dissolution of $CaCO_3$. These possible explanations might also explain the subtle, but steady increase in $CaCO_3$ content that occurs from about 2500 to 3650 m water depth. Finally, the 20% increase of $CaCO_3$ content which occurs over the water depth range of 1600 to 2000 m corresponds to the transition from AAIW to underlying NADW. The saturation state of seawater with respect to $CaCO_3$ minerals is slightly greater in NADW than AAIW (Figure 9).

During the Last Glacial Maximum (LGM), i.e., in MIS 2, a similar trend of greater $CaCO_3$ content with greater water depth exists, measurements range from 26 to 69% with a maximum $CaCO_3$ content at a water depth about 1700 m (converted to MIS 2 water depths) is seen in the Walvis Ridge cores (Figure 10b). The Cape Basin cores

have a lower measured $CaCO_3$ content ranging from 28 to 47% with a maximum at a water depth about 1800 m. However, at both sites the $CaCO_3$ content is lower compared to Late Holocene core top data.

The LGM $CaCO_3$ content profiles can be interpreted with the current understanding of LGM water mass distributions (see Figure 1, Curry and Oppo, 2005). During the LGM, the boundary between AAIW and upper NADW (referred to as GNAIW during the LGM) was shallower than it is now. More $CaCO_3$ saturated waters would therefore have occupied the same position as less saturated waters in today's ocean, which would have allowed a greater amount of $CaCO_3$ to accumulate on the seafloor between 1700 and 1900 m. During the LGM, the southern-sourced deep waters (referred to as Antarctic Bottom Water, or AABW) occupied the position of the core of NADW in today's ocean, centered at about 3000 m. If AABW was much less saturated with respect to $CaCO_3$ than GNAIW, then a lower amount of $CaCO_3$ would have accumulated on the seafloor at AABW depths (i.e., depths greater than 2500 m). Consistent with this scenario, LGM $CaCO_3$ contents are not as high as late Holocene values.

It is interesting to consider the temporal relationship between the changes in $CaCO_3$ content and climate (as indicated by $\delta^{18}O$) during the time period spanned MIS 2 to MIS 1. A relative minimum in $CaCO_3$ content occurs ~22.5 kya while the relative maximum in $\delta^{18}O$ occurs ~18-20 kya; the minimum in $CaCO_3$ precedes the maximum in $\delta^{18}O$ by ~3.5 kyr. This offset is observed in all of the paired $CaCO_3$ and $\delta^{18}O$ profiles

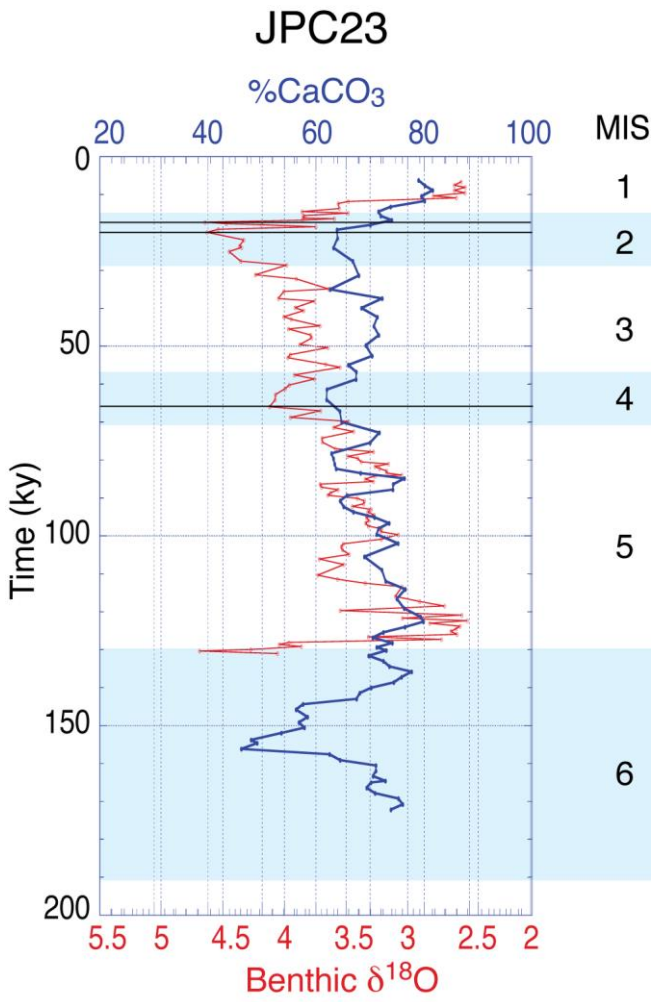

Figure 11. $CaCO_3$ offset compared to $\delta^{18}O$ during LGM due to the $CaCO_3$ preservation spike in example core JPC23. The black lines highlight offset from $\delta^{18}O$ (red) and $CaCO_3$ content (blue).

obtained from our Namibia cores, example in Figure 11. This offset is consistent with the occurrence of an aragonite preservation spike at the boundary between MIS 1 and MIS 2, such as has been reported in cores from both the Atlantic and Pacific Oceans (see Berger, 1977). The preservation spike has been attributed to the global marine carbonate system's adjustment to changes in the atmospheric and oceanic inorganic carbon reservoirs (e.g. Broecker, 1981). Along the southwest African margin, temporal variations in sedimentary $CaCO_3$ content may also be influenced by temporal variations of the positions of water masses and the influx of non-$CaCO_3$ sediments.

4.4 Sedimentation and Mass Accumulation Rates

Several possible influences on $CaCO_3$ content exist. To better constrain how significant each of these influences might be, we considered how sedimentation and mass accumulation rates varied spatially and temporally.

Figure 12 shows calculated whole-core average sedimentation rates versus water depth. Cores from the Walvis Ridge region show the following: over the depth range of 550 to 1100 m sedimentation rates exceed 10 cm/ky, over the depth range of 1800 to 3200 m sedimentation rates fall in a limited range of 4.6 to 6.3 cm/ky, and at depths greater than 3200 m sedimentation rates are 4.3 to 4.6 cm/ky, which are the lowest values found. Cape Basin cores were recovered from the limited water depth range of 2200 to 2650 m; their whole-core average sedimentation rates decrease with increasing water depth from 7.3 to 5.6 cm/ky. These values are like those from the Walvis Ridge region cores from similar water depths.

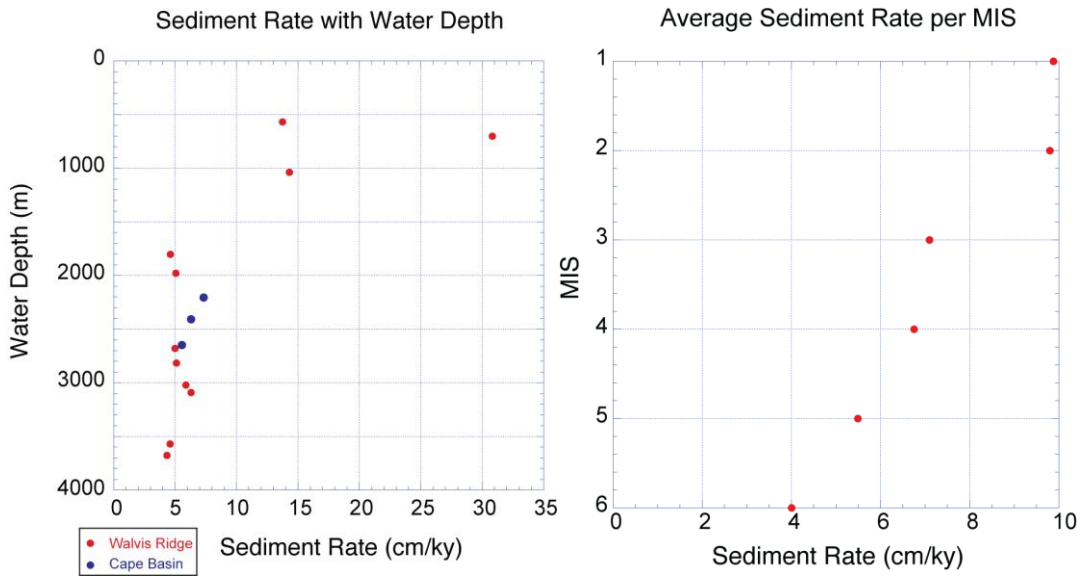

Figure 12. (a) Average sediment rate for each core with water depth. Walvis Ridge (red), Cape Basin (blue). (b) The average sediment rate for each marine isotope stage, Cape Basin rates were averaged into the total sediment rate for each marine isotope stage.

The sedimentation rate of each MIS was also calculated and there is an observed decrease in the sedimentation rate with increasing age (Figure 13). From MIS 1 through MIS 6, sedimentation rates decrease steadily from 9.87 to 4.0 cm/kyr, though sedimentation rates for MIS 1 and 2 are very similar (9.87 and 9.80 cm/kyr, respectively). This decrease of sedimentation rate reflects the progressive compaction of the sediments over time, which caused time horizons in the sediments to become more closely spaced[2]. Thus, there is some ambiguity to the significance of sedimentation rates in and of themselves.

We therefore calculated mass accumulation rates (MARs), which involved the use of both sedimentation rate and sediment bulk density values. The effect of compaction on the sedimentation rates was compensated for by an associated increase in the bulk densities of the sediments. MARs were calculated using the following relationships:

MAR_{total} = sedimentation rate * dry bulk density

MAR_{CaCO3} = sedimentation rate * dry bulk density * $CaCO_3$ content / 100

$MAR_{non\text{-}CaCO3}$ = sedimentation rate * dry bulk density * (100 - $CaCO_3$ content) / 100

where MAR_{total} is the mass accumulation rate of total sediment, MAR_{CaCO3} is the mass accumulation rate of $CaCO_3$, and $MAR_{non\text{-}CaCO3}$ is the mass accumulation rate of non-$CaCO_3$ sediment. Dry bulk density was derived from the total bulk density of the

[2] To some extent, the decrease in whole-core sediment rate values may also reflect a slight sampling bias. All cores were similar in length. So, when sedimentation rates were high during MIS 1-3 no sediments from MIS ≥3 were recovered, and when sedimentation rates were low during MIS 1-3 sediments from MIS ≥3 were recovered.

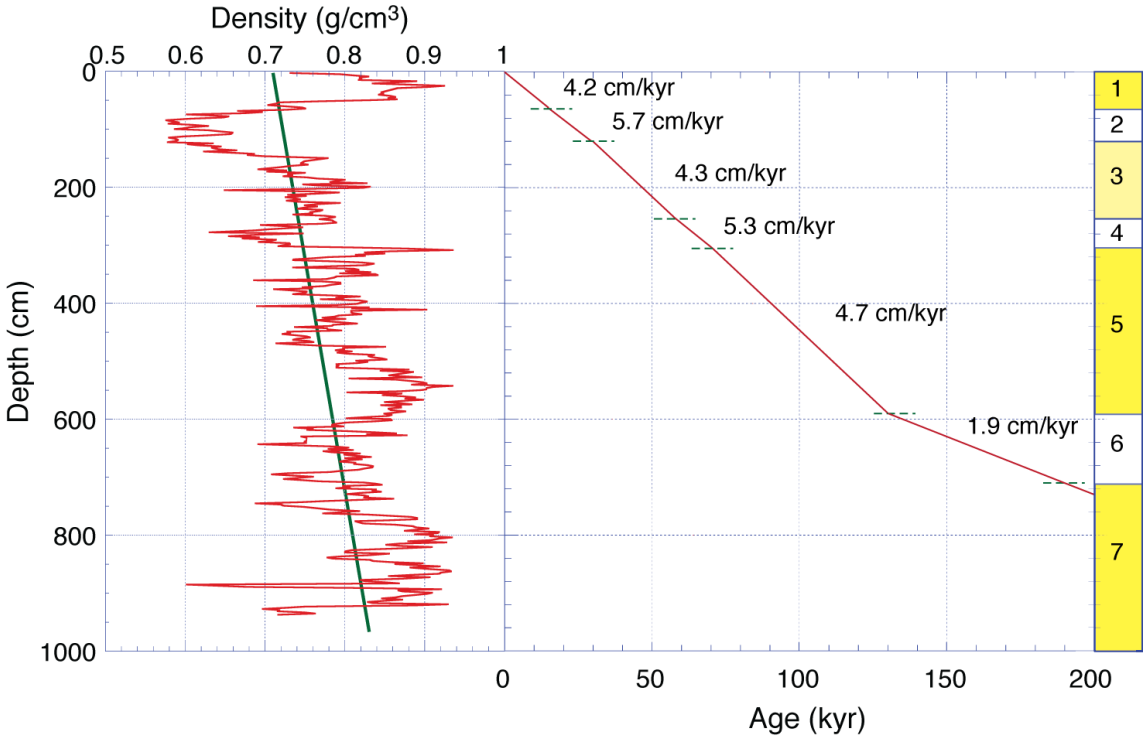

Figure 13. Sedimentation rate for JPC49. It can be observed the sedimentation rate does decrease with depth; however, the dry bulk density increases.

sediment measured by the MSCL assuming that the sediment grains had a density of 2.68g/cm^3 and the water had a density of 1.024 g/cm^3, which correspond to typical sediments and ambient seawater.

MARs in cores from water depths less than 1400 m differ in two fundamental ways from MAR values in cores from greater water depths. MAR_{total}, MAR_{CaCO3} and $MAR_{non\text{-}CaCO3}$ values for each marine isotope stage are shown in Figure 14 versus depth. Above 1400 m, MAR values are several times greater than MAR values in cores from greater depths. Also, at 1400 m depth there is a shift in the relative dominance of MAR_{CaCO3} and $MAR_{non\text{-}CaCO3}$ such that in shallower cores non-$CaCO_3$ material make a greater contribution to the MAR_{total} whereas in deeper cores $CaCO_3$ material make a greater contribution.

During MIS 1 in the Walvis Ridge, the total mass accumulation rate varies significantly with depth, the highest and lowest calculated MAR_{total} are at about 700 and 3100 m water depth with values of 27.54 and 3.5 g/cm^2/kyr, respectively. The average MAR_{total} for MIS 1 is 5.91 g/cm^2/kyr. There is slightly greater MAR_{total} in the water depth range of about 1700 to 2800 m compared to just above and below this water depth range. These changes in MAR_{total} may reflect water mass geometry. With the slightly higher MAR_{total} in the water depth range 1700 to 2800 m being attributed to NADW, and the lower MAR_{total} at shallower and deeper water depths could be associated with southern-sourced waters. During the LGM, in MIS 2, a minimum MAR_{total} is observed at about 1860 m water depth of 1.9 g/cm^2/kyr. The MAR_{total} at all other water depths has an average of 5.6 g/cm^2/kyr. A maximum MAR_{total} is observed at about 600 m water depth

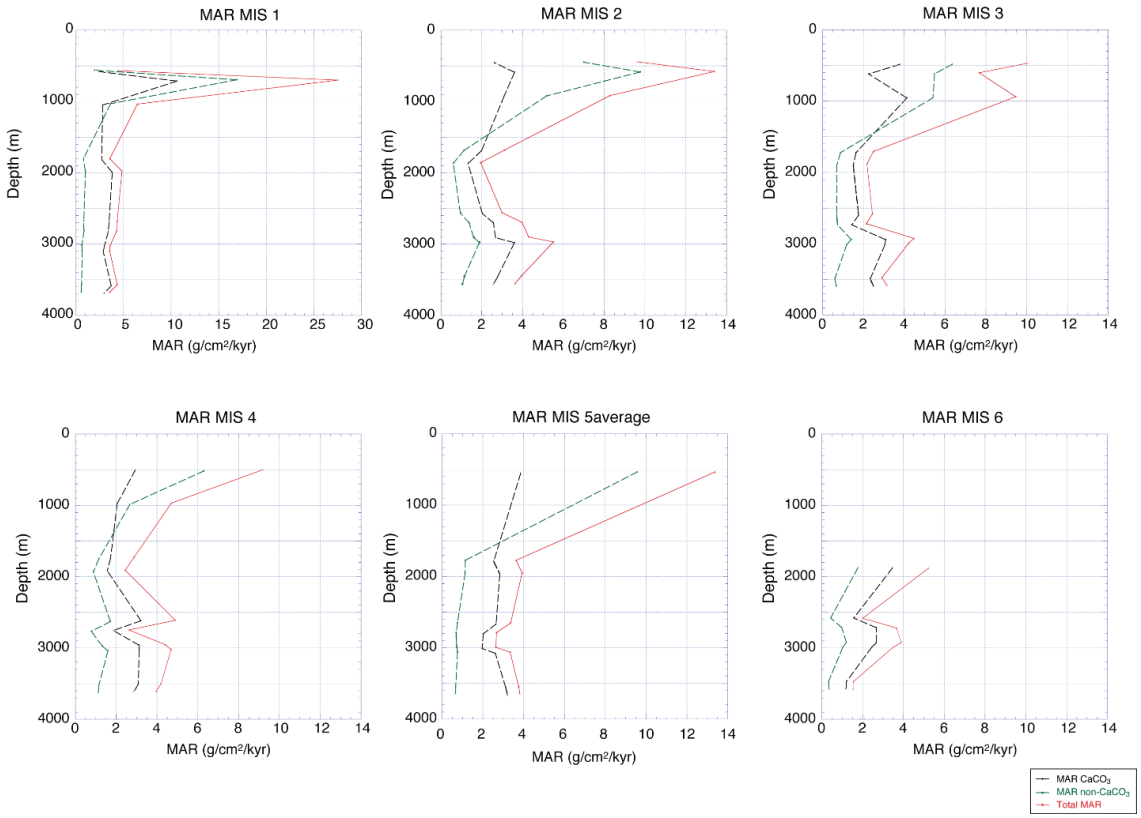

Figure 14. Mass accumulation rates divided by the marine oxygen isotope stage with depth. The black horizontal line in each of the plots indicate the water depth where the MAR transitions from non-$CaCO_3$ dominated sediment to $CaCO_3$ dominated sediment.

of 13.41 g/cm^2/kyr. There is an increase in MAR_{total} from 2600 to 3000 m, with the average MAR_{total} for the LGM being 5.4 g/cm^2/kyr.

What are the environmental processes that produce the variations of sediment mass accumulation rate? Figure 14 shows that the very high MAR_{total} that occur in the three shallowest cores result primarily from high $MAR_{non\text{-}CaCO3}$. For example, during MIS 2 $MAR_{non\text{-}CaCO3}$ comprises from 65 to 75% of MAR_{total}; importantly, MAR_{CaCO3} in the shallow cores are similar in magnitude to the MAR_{CaCO3} in the other cores. Riverine influx of non-$CaCO_3$ sediment to the Namibian continental shelf and slope is minimal. Aeolian processes are known to transport terrigenous sediment from Namibia nearly 1500 km out over the ocean (Shannon and Anderson, 1982). NASA imagery illustrates distinct plumes of terrigenous sediment from the arid interior of southern Africa being transported offshore of the Namibian continental shelf and slope by strong winds (Figure 15).

The presence of quartz, a typical wind-blown mineral, is indicated by the results of our XRD analyses. Figure 16 shows the relative abundances of quartz in cores JPC58 and JPC13, which are from shallow and deep water, respectively. The relative abundance is about 2-3 times greater in the shallow core and the relative MAR of quartz of is about 4 times greater in the shallow core. Quartz deposition significantly dilutes the $CaCO_3$, explaining the low $CaCO_3$ contents measured in both shallow and deep cores (Figure 8). The relative abundances and MAR of quartz are also greater during glacial periods compared to interglacial periods. During modern times significant aeolian transport occurs during winter when the South Atlantic High pressure cell resides

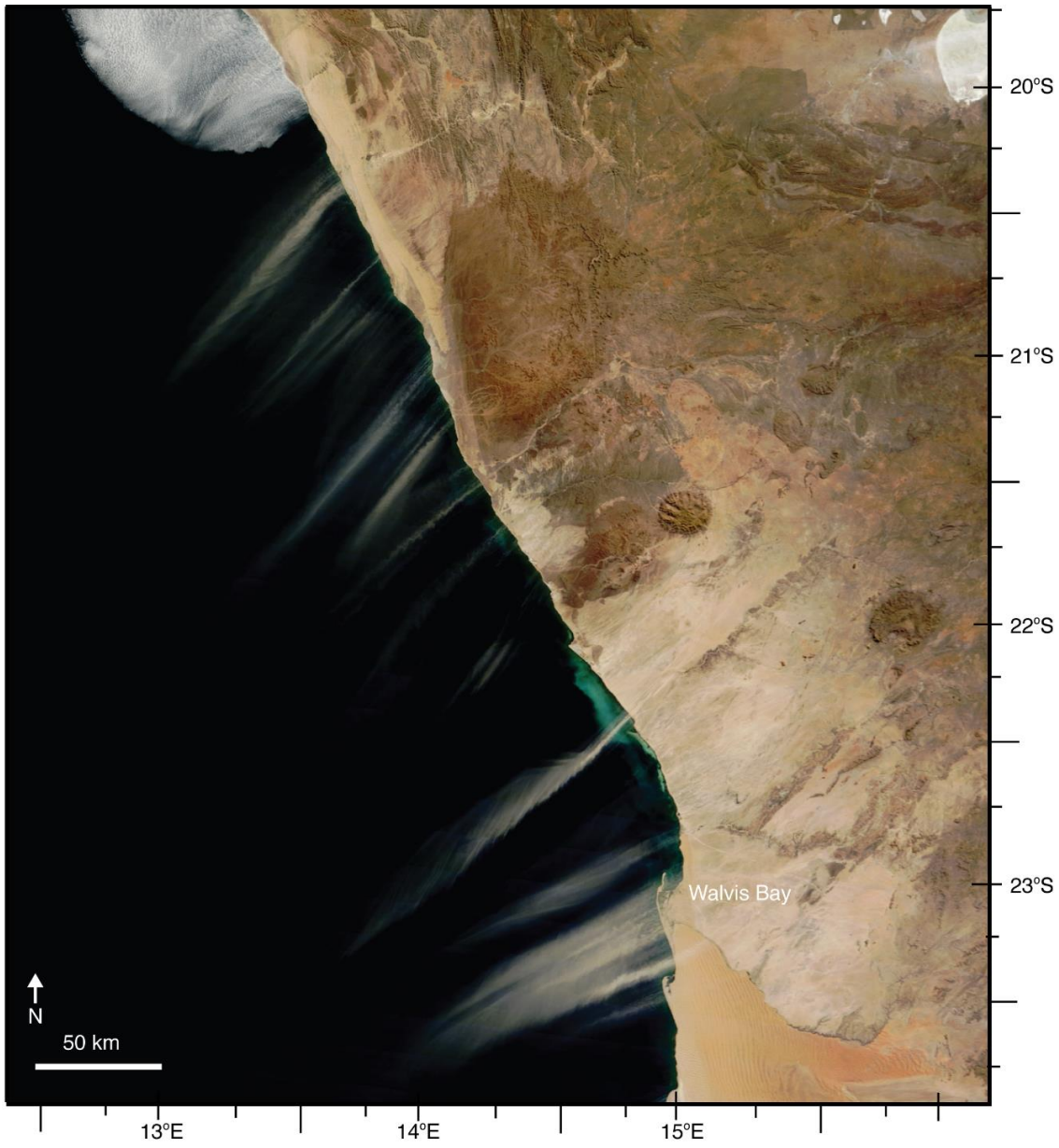

Figure 15. Aeolian transport from Namibia over the Atlantic Ocean. Modified after NASA image by Schmaltz (2015).

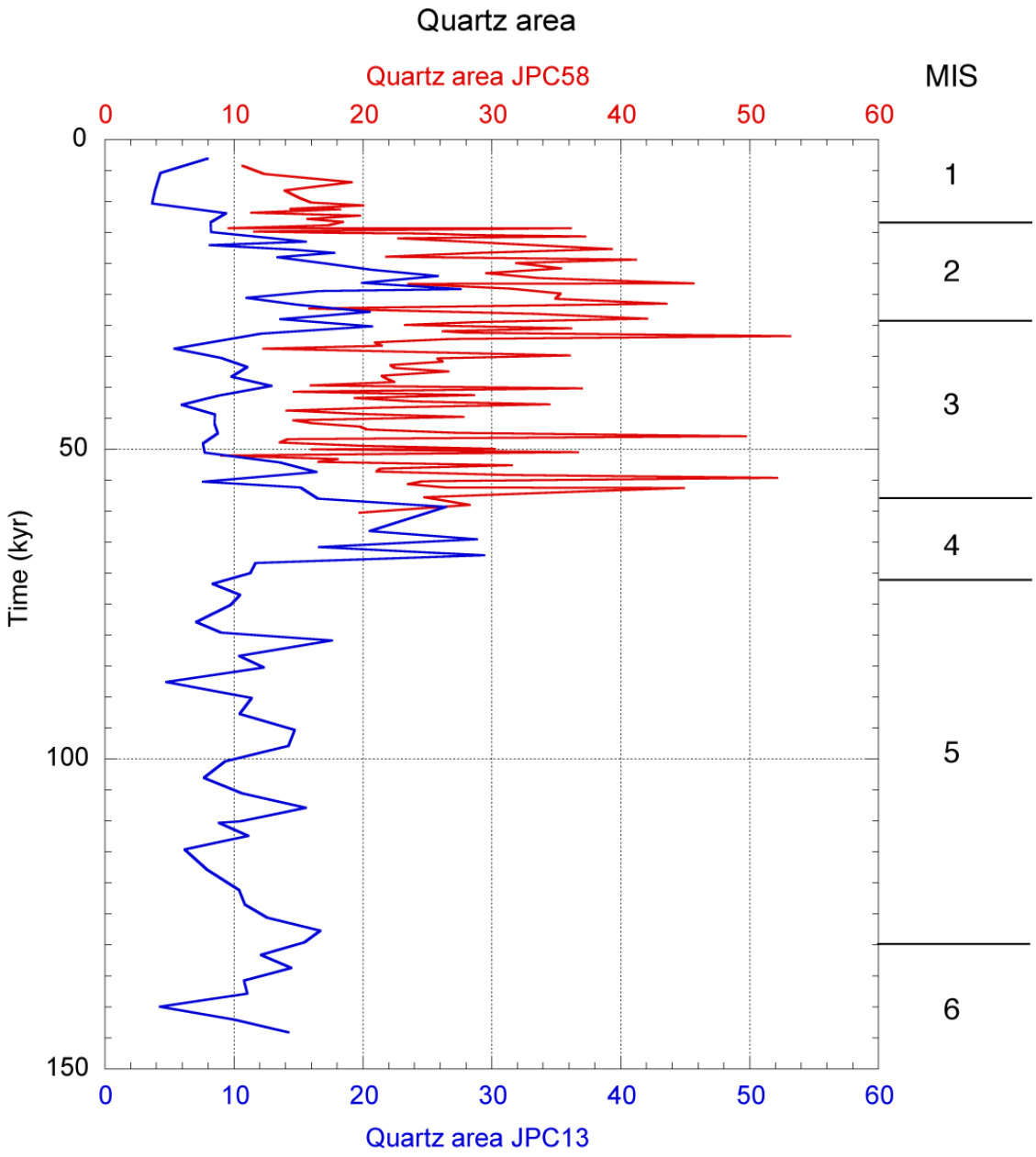

Figure 16. The presence of quartz seen in XRD data. Shallow core JPC58 red line, water depth 1037 m, has a relative MAR of 4 times more quartz abundance compared to deeper core JPC13 blue line, located at 3092 m.

offshore of southwest Africa and another high pressure cell resides over the African subcontinent (Nelson & Hutchings, 1983) and hot and dry continental conditions drive strong Berg winds, which transport sediment offshore (Shannon, 1985). Shannon (1985) suggests that during the LGM, a continuous high pressure cell resided over the African subcontinent and the positions of the high pressure cells changed, and that caused drier and warmer continental conditions and increased aeolian transport (Figure 17).

What are possible explanations for the relative maximum in MAR that occurs between 2600 to 3000 m during MIS 2 (Figure 14). This maximum does not appear to be an artifact caused by the where we chose to locate the MIS boundaries. One possible explanation is localized topographically-induced sediment focusing along the Namibian margin (e.g., Mollenhauer et al., 2001). Alternatively, as the feature is apparent in cores at similar depths but different locations along the margin, it may reflect a regionally prevalent cause – the location of the boundary between water masses. As the horizontal velocity of waters at the transition between northern-sourced GNIAW and southern-sourced CDW approaches zero, the likelihood of suspended sediment grains being deposited on the seafloor and MAR would have increased.

In the modern ocean, differences exist between the circulation of NADW in the eastern and western sides of the South Atlantic Ocean and its geometry relative to southern-ocean sourced water masses (see review by Reid, 1994). The primary influx of NADW occurs as boundary flow along the ocean basin's western margin, where relatively distinct boundaries exist between NADW and the southern-sourced water masses. The influx of NADW is much weaker and more diffuse in the eastern side of the

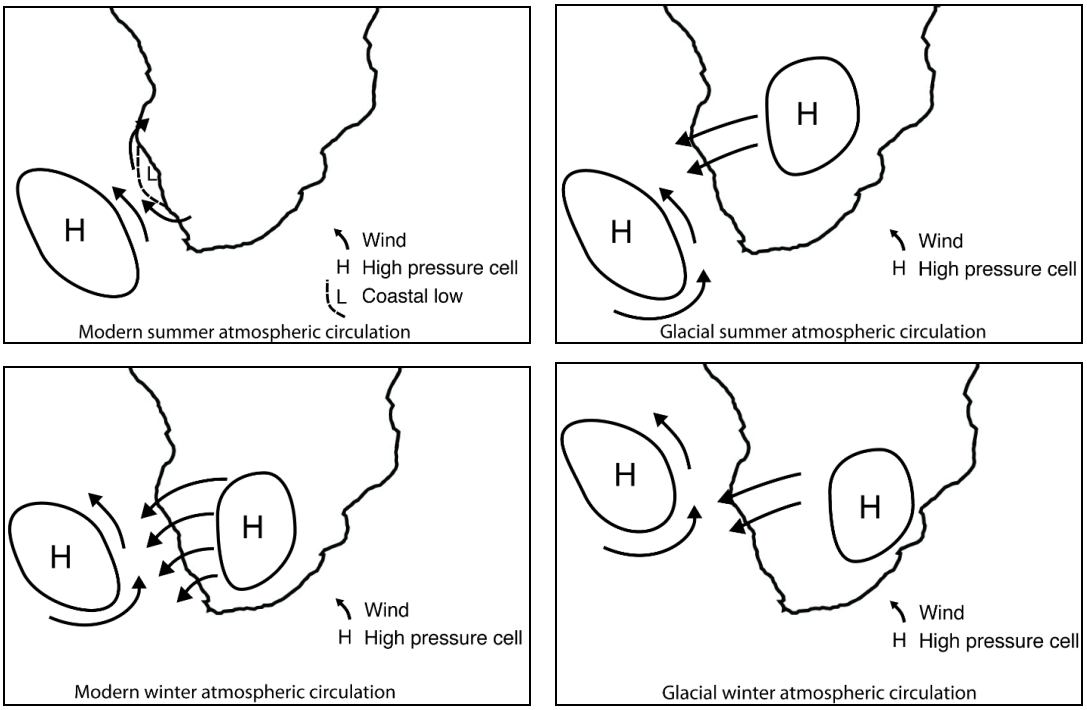

Figure 17. Atmospheric high pressure systems. Left. Modern summer and winter atmospheric high pressure systems. The high pressure over the African subcontinent causes drier continental conditions and stronger offshore wind. Right. LGM summer and winter atmospheric high pressure systems, similar to modern winter conditions which would cause drier continental conditions and stronger offshore winds. Figures modified from Nelson & Hutchings (1983) with added information from Shannon (1985).

basin. How did the circulation and geometry of water masses in the eastern side of the basin compare with those in the western side during MIS 2?

There are almost no published results for eastern basin water mass geometry. In Figure 18 the modern water masses and Curry and Oppo, 2005, defined water mass boundaries are overlain on MIS 1 and MIS 2 MAR plots, respectively. As noted above, the water boundaries differ between the eastern and western sides of the South Atlantic basin. This would create an offset in the water mass boundaries represented in Curry and Oppo, 2005 for the eastern basin of the South Atlantic. However, with our sedimentary $CaCO_3$, MAR_{total}, MAR_{CaCO3} and $MAR_{non\text{-}CaCO3}$ along the Namibian margin and complementing work done by Marchitto and Broecker, 2006; and Marson et. al, 2016, we give a better understanding of the LGM water masses along the east South Atlantic Ocean; inferences of water mass geometry for the eastern basin of the South Atlantic Ocean can be constrained. During the LGM, southern-sourced AAIW would be shallower than it is today, this would allow more $CaCO_3$ to accumulate between 1400 and 1900 m water depth in today's oceans, so the AAIW would have been above 1600 m during the LGM. Southern-sourced bottom water (AABW) would be much less saturated in $CaCO_3$ compared to GNAIW, lower amounts of $CaCO_3$ are recorded at depths greater than 2600 m. This would have GNAIW fill the intermediate depths of about 1400 to 2600 m in this region.

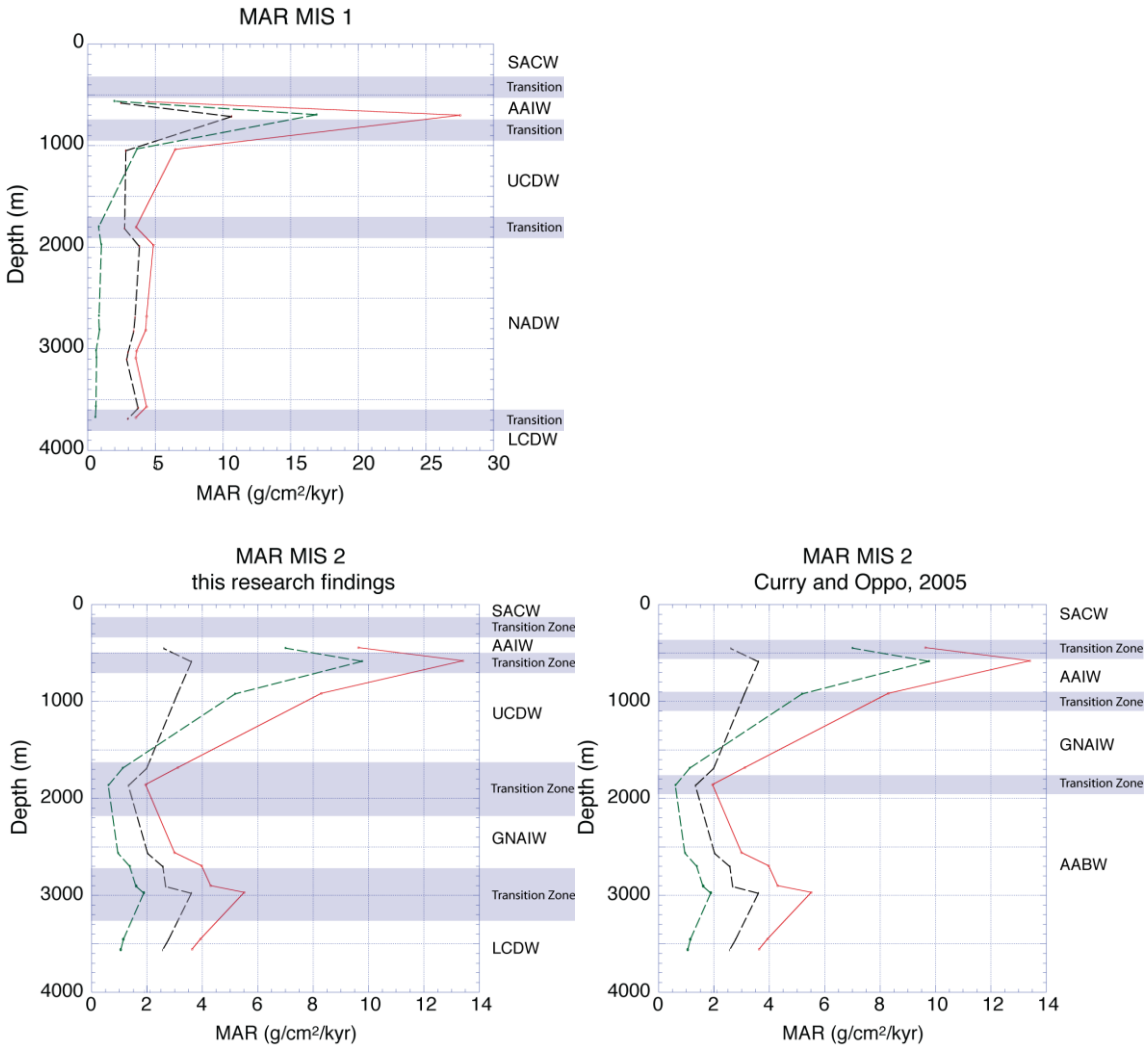

Figure 18. MAR_{total}, MAR_{CaCO3}, and $MAR_{non\text{-}CaCO3}$ for MIS 1 and MIS 2. (a) MIS 1 of MAR_{total}, MAR_{CaCO3}, and $MAR_{non\text{-}CaCO3}$ with overlaid modern water masses as defined by SODAsi.3 and WOCE. (b) MIS 2 of MAR_{total}, MAR_{CaCO3}, and $MAR_{non\text{-}CaCO3}$ with revised overlaid LGM water masses from results from this paper. (c) MIS 2 of MAR_{total}, MAR_{CaCO3}, and $MAR_{non\text{-}CaCO3}$ with overlaid LGM water masses as defined by Curry and Oppo, 2005. MAR_{total}, MAR_{CaCO3}, and $MAR_{non\text{-}CaCO3}$ are indicated by red, black, and green lines, respectively.

The rates at which seafloor $CaCO_3$ dissolution occurs at various water depths (D_{min}) can be estimated based upon the differences between MAR_{CaCO3} at shallow and deep core sites[3] (Curry & Lohmann, 1986). We took shallow core sites to be those that occur in water depths above the modern aragonite lysocline, the top of which is at or above 1000 m. Figure 19 shows estimates of seafloor $CaCO_3$ dissolution along the continental slope of the Namibian margin obtained this way. During MIS 1, dissolution rates at depths greater than 1500 m ranged between 1.5 and 2.5 g/cm^2/kyr. Since MAR_{CaCO3} values at these depths were 3.3 g/cm^2/kyr, about 31 to 43% of the $CaCO_3$ originally deposited on the seafloor has dissolved. In comparison, during MIS 2 dissolution rates at depths greater than 1500 m were less than 0.6 g/cm^2/kyr in all but one instance; however, two negative dissolution rate values exist. Given the overall consistency of the D_{min} values with depth during MIS 2, we infer that, regardless of the geometry of water masses, the vertical profile of seawater carbonate saturation state was such that the deeper cores were below the aragonite lysocline and above the calcite lysocline. The occurrence of the negative values suggest dissolution at the shallow water sites may have occurred, which would bias the estimates at deep sites. Such dissolution could have occurred during MIS 2 if AAIW was more corrosive with respect to aragonite, or if the flux of organic matter to the seafloor was greater. Wefer et al., 1996, suggest that biological productivity in sea surface along the Namibian margin was

[3] The seafloor dissolution rate (D_{min}) is $MAR_{CaCO3\ SHALLOW}$ minus $MAR_{CaCO3\ DEEP}$ if little downslope transport and dissolution of $CaCO_3$ at shallow water sites occurs. If shallow-water dissolution does occur then the estimates are minimum values.

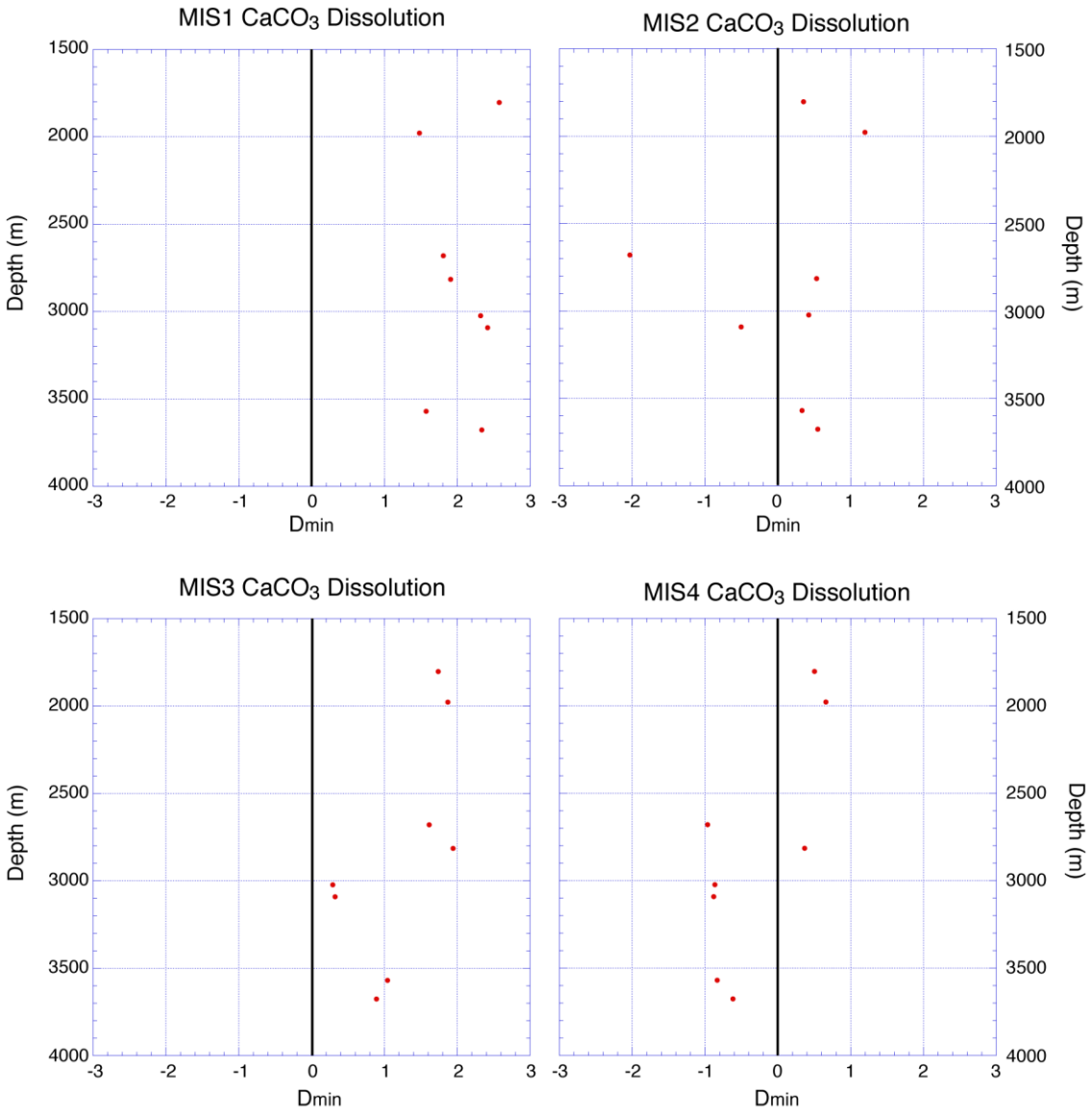

Figure 19. D_{min} for each marine isotope stage 1-4. Positive numbers indicate dissolution in the sediment at that depth where negative numbers indicate deposition of $CaCO_3$ sediment at those depths.

substantially greater during MIS 2, this would account for the higher preservation seen in the deep cores.

4.5 $CaCO_3$ Contents and Mass Accumulation Rates during Marine Isotope Stages 3 through 6

In addition to the information about the MIS 1 and 2, several of the Nambian sediment cores provided information about sedimentary and oceanographic conditions in the depth range of 450 to 3700 m during time period corresponding to MIS 3 through MIS 6 (see Figure 20), which correspond to the early part of the last glaciation, the last interglacial, and the penultimate glaciation, respectively. During the older MIS, the minimum $CaCO_3$ content, in range of 25-30%, consistently occurs near 700 m. $CaCO_3$ contents generally increase with water depth from 450 to 3700 m (except during MIS 1 and 5e, values from the Walvis Ridge region are about 15% greater than those from the Cape Basin region), though the $CaCO_3$ contents increase at a lower rate below 2000 m.

Figure 20 shows the average $CaCO_3$ content for each MIS that was calculated for all cores. The highest average $CaCO_3$ contents (>70%) occurred during MIS 1, 5, and 6 (a sampling bias may exist for MIS 6, it was only recorded in cores deeper than 2000 m). Sediments corresponding to interglacial MIS 1 and 5 exhibit greater $CaCO_3$ contents than those associated with glacial MIS 2, 4, and 6, and MIS 3 has intermediate $CaCO_3$ content values (Figures 7, and 20). The reasons for these patterns are as discussed above for MIS 1 and 2.

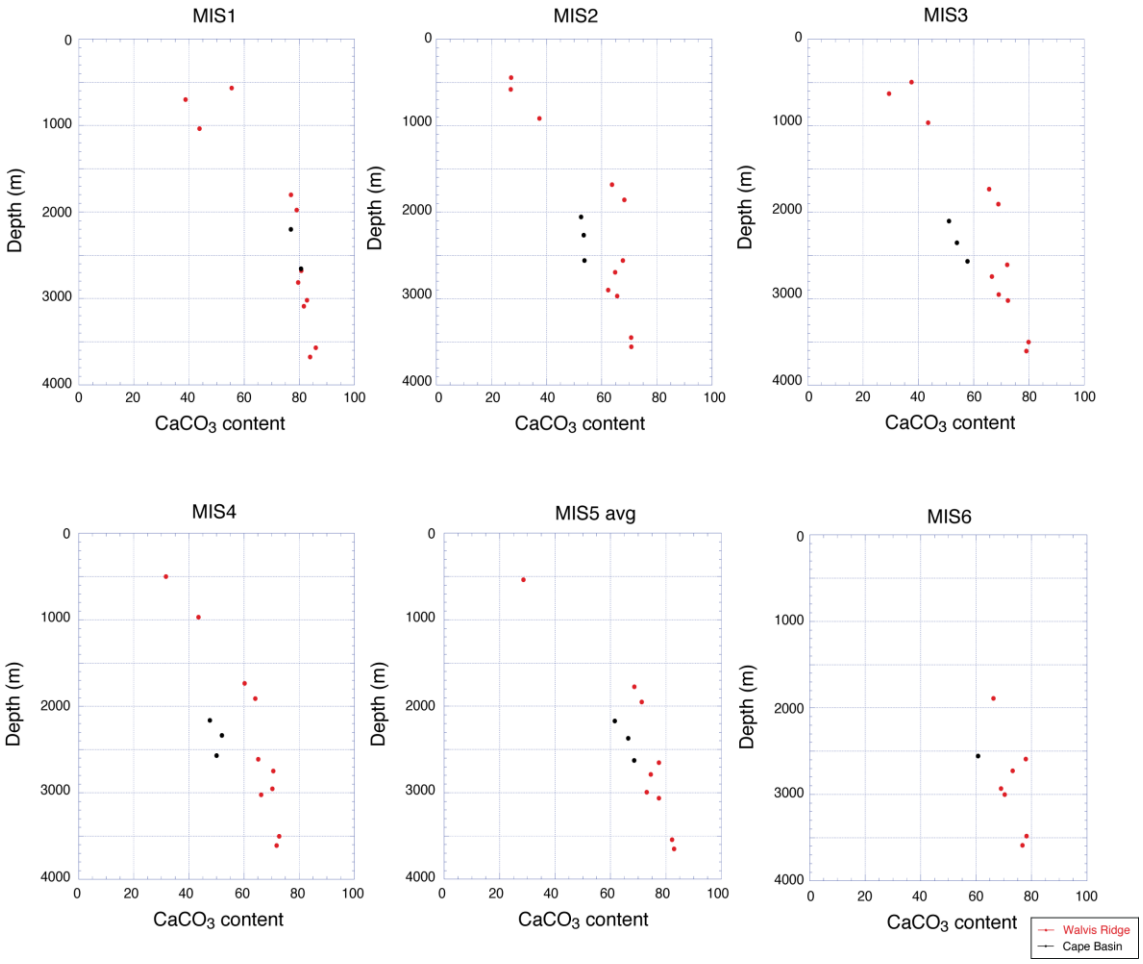

Figure 20. $CaCO_3$ content versus water depth for each MIS. Walvis Ridge (red) and Cape Basin (black) $CaCO_3$ plots versus depth. The two different locations are similar in MIS 1 and MIS 5avg with differences being seen in MIS 2 through 4.

Figure 21 shows that at the Walvis Ridge region the greatest values of MAR_{total} during each MIS occur at water depths shallower than 1100 m (27.5, 12.4, 10.0, 9.2, and 13.4 g/cm^2/kyr for MIS 1-5, respectively), reflecting the proximity to carbonate and silica derived from the Benguela upwelling system and terrigenous sediments derived from continental Africa. From 1100 to 3650 m water depth, values of MAR_{total} occur within the limited range of 1.5 to 5.5 g/cm^2/kyr during all MIS. The magnitudes of MAR_{total} and ranges of MAR_{total} are less than at depths shallower than 1100 m; nevertheless, significant variations in the patterns of MAR_{total} versus depth do occur. During interglacial MIS 1 and 5 are similar, with a slight relative minimum (~0.7 g/cm^2/kyr less than adjacent values) occurring in the cores from the water depth range of about 2700 to 3100 m (Figure 21a), and during glacial MIS 2, 3, 4, and 6 are similar to each other, with a relative maximum (~1.4 g/cm^2/kyr greater than adjacent values) occurring in the cores from the water depth range of about 2700 to 3000 m. Of these two features, the latter is most prominent; it is consistent with the occurrence of the boundary between northern-sourced GNAIW and southern-sourced CDW (see discussion above).

4.6 Dissolution Rates

Estimated rates of dissolution of $CaCO_3$ on the seafloor during MIS 3 and MIS 4 are shown in Figure 18. The patterns of dissolution with depth during MIS 3 and 4 are similar to each other. Relatively high rates of dissolution occur above 2000 m and relatively low rates occur below 3000 m. During MIS 3, the transition between high and low rates occurs in at 2900 m; it is not possible to precisely determine the depth of the

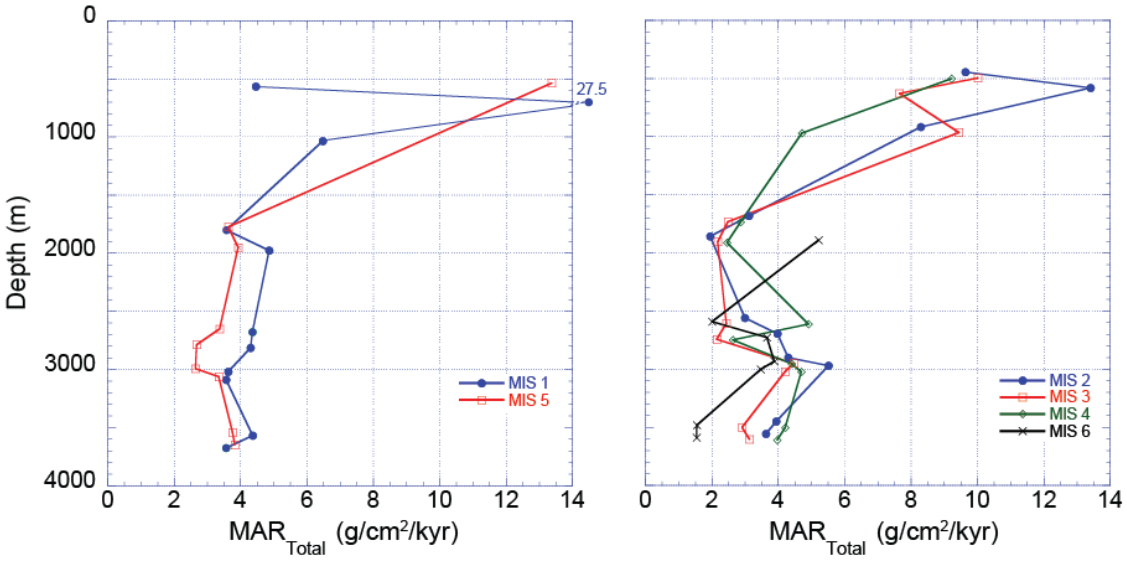

Figure 21. MAR_{total} during each MIS versus water depth. Depths have been corrected to account for the differences between modern sea-level and sea level during each MIS.

transition during MIS 4. The MIS 3 and MIS 4 profiles display a more distinct transition than is evident in MIS 2. It is worth noting that the transition cannot be caused simply by the effect of increasing pressure with depth on the carbonate saturation state of seawater, because if this happened, dissolution would increase with depth, not decrease. Therefore, the depth of the transition is consistent with a change in seawater carbonate saturation state due to a change in water mass.

5. SUMMARY AND CONCLUSIONS

The deposition of $CaCO_3$ and other sediment types on the seafloor of the continental slope of Namibia vary spatially and temporally. The $CaCO_3$ content (weight percent) generally increases with water depth. The $CaCO_3$ content also varies directly with interglacial-glacial stages such that lowest $CaCO_3$ contents occur during glacial MIS 2, 4 and 6, and the highest $CaCO_3$ contents occur during interglacial MIS 1 and 5. Variations in MAR_{total}, MAR_{CaCO3} and $MAR_{non\text{-}CaCO3}$ indicate that these differences are primarily due to greater input of non-$CaCO_3$ sediment during glacial periods, rather than dissolution of $CaCO_3$ on the seafloor. The depth distributions of $CaCO_3$ content and MAR_{CaCO3} in sediments corresponding to the late Holocene are consistent with the vertical distributions of intermediate and deep water masses in the eastern South Atlantic Ocean today.

Comparison of the depth distributions of $CaCO_3$ content and MAR_{CaCO3} corresponding to MIS 1 and MIS 2 suggest that AAIW is present at water depths ranging from 500 to 1100 m, NADW is present at water depths of about 1400 to 2600 m and southern sourced bottom water fills the remaining basin up to 3100 m water depth. As seen in Figure 18 there are transition zones between water masses, this is to allow for mixing and the uncertainty of depths. During MIS 2, the geometry of water masses in the eastern side of the South Atlantic Ocean are different compared to those in the western side of the basin. On the eastern side of the South Atlantic AAIW has a core water depth of about 750 m, NADW core is near 2000 m and CDW/AABW resides below 3100 m.

In the western side of the South Atlantic Ocean the AAIW core is 700 m, NADW 1400 m and CDW/AABW fills the bottom up to a water depth of 2000 m.

The results presented here suggest several lines of future work might be fruitful. Both deposition of aeolian sediments and biological productivity associated with the coastal upwelling system are influenced by the atmospheric high pressure systems near Namibia. The history of this aspect of the climate system might be reconstructed based upon analysis of variations of sediment mineralogy and organic carbon in marine sediments along the southwest African margin. Also, it is implicitly assumed that the glacial water masses had chemical properties, such as carbonate saturation state, which are similar to those of modern water masses. Further analyses of paleoceanographic proxies, such as carbon isotopes, boron isotopes and Cd/Ca of foraminifera would yield information about how the chemical properties of the main water masses in this region varied through time. Note: aspects of this research are being pursued now.

REFERENCES

Anderson, D. and Archer, D. (2002). Glacial-interglacial stability of ocean pH inferred from foraminifer dissolution rates. *Nature, 416*, 70-73.

Archer, D. and Maier-Reimer, E. (1994). Effect of deep-sea sedimentary calcite preservation on atmospheric CO2 concentration. *Nature, 367*, 260–263.

Bacon, M. (1984). Glacial to interglacial changes in carbonate and clay sedimentation in the Atlantic Ocean estimated from ^{230}Th measurements, *Isotope Geoscience, 2*, 97-111.

Balsam, W. and McCoy, F. (1987). Atlantic sediments: Glacial/Interglacial comparisons. *Paleoceanography, 2*, 531-542.

Berger, W. (1973). Deep-sea carbonates: Pleistocene dissolution cycles. *Journal of Foraminiferal Research, 3,* 187-195.

Berger, W. (1977). Deep-sea carbonate and the deglaciation preservation spike in pteropods and foraminifera, *Nature, 269,* 301-304.

Bickert, T. and Wefer, G. (1996). Late Quaternary Deep Water Circulation in the South Atlantic: Reconstruction from Carbonate Dissolution and Benthic Stable Isotopes. In: Wefer, G., Berger, W., Siedler, G. and Webb, D. (eds), *The South Atlantic: Present and Past Circulation.* Springer-Verlag Berlin Heidelberg, 599-620.

Bremner, J.M. (1981). Shelf morphology and surficial sediment off Central and Northern South West Africa (Namibia). *Geo-Marine Letters, 1*, 91-96.

Broecker, W. and Broecker, S. (1974) Carbonate dissolution on the Western flank of the East Pacific Rise, *The Society of Economic Paleontologists and Mineralogists (SEPM) Studies in Paleo-Oceanography*, 44-57.

Broecker, W. (ed) (1981). Glacial to Interglacial Changes in Ocean and Atmosphere Chemistry. In: *Climatic Variations and Variability: Facts and Theories*, D. Reidel Publishing Company, 111-121

Broecker, W. and Peng, T. (eds) (1982). *Tracers in the Sea.* Columbia University, Palisades, New York: Lamont-Doherty Geological Observatory.

Crowley, T. (1985). Late Quaternary Carbonate Changes in the North Atlantic and Atlantic/Pacific Comparisons. In: Sunquest, E., Broecker, W. (eds), *The Carbon Cycle and Atmospheric CO_2: Natural Variations Archean to Present.* AGU, Washington, D. C., 271-284.

Curry, W. and Lohmann, G. (1986). Late Quaternary carbonate sedimentation at the Sierra Leone Rise (Eastern Equatorial Atlantic Ocean). *Marine Geology, 70*, 223-250.

Curry, W. and Oppo D. (2005). Glacial water mass geometry and the distribution of δ13C of ΣCO2 in the western Atlantic Ocean. *Paleoceanography, 20*, 1-12.

Diester-Haass, L., Heine, K., Rothe, P. and Schrader, H. (1988). Late Quaternary history of continental climate and the Benguela Current off South West Africa. *Paleogeography, Paleoclimatology, Paleoecology, 65*, 81-91.

Duplessy, J., Shackleton, N., Fairbanks, R., Labeyrie, L., Oppo, D. and Kallel, N. (1988). Deepwater source variations during the last climatic cycle and their impact on the global deepwater circulation. *Paleoceanography 3,* 343-360.

Emerson, S. and Archer, D. (1990). Calcium carbonate preservation in the Ocean. *Philosophical Transactions of the Royal Society of London A 331,* 29-40.

Emery, W. and Meincke, J. (1986). Global water masses-summary and review. *Oceanologica Acta, 9.4,* 383-391.

Emiliani, C. (1955). Pleistocene temperatures. *The Journal of Geology, 63,* 538-578.

Farrell, J. and Prell, W. (1989). Climatic change and $CaCO_3$ preservation: An 800,000-year bathymetric reconstruction from the central Equatorial Pacific Ocean. *Paleoceanography, 4,* 447-466.

Freeman, E., Skinner, L., Waelbroeck, C. and Hodell, D. (2016). Radiocarbon evidence for enhanced respired carbon storage in the Atlantic at the Last Glacial Maximum. *Nature Communications, 7:11998* doi:10.1038/ncomms11998

Giresse, P. (ed.) (2008). *Tropical and Sub-Tropical West Africa Marine and Continental Changes During the Late Quaternary.* Amsterdam, The Netherlands: Elsevier.

Hays, J., Saito, T., Opdyke, N., and Burckle, L. (1969). Pliocene-Pleistocene Sediments of the equatorial Pacific: Their paleomagnetic, biostratigraphic, and climatic record. *Geological Society of America Bulletin, 80,* 1481-1514.

Huhn, K., Paul, A., Seyferth, M. (2007). Modeling sediment transport patterns during an upwelling event. *Journal of Geophysical Research, 112,* C10003.

Huneke, H. and Henrich, R. (2011). Pelagic sedimentation in modern and ancient oceans. *Developments in Sedimentology, 63,* 215- 351. doi:10.1016/S0070-4571(11)63004-5

Jansen, J., Van der Gaast, S., Koster B., and Vaars, A. (1998). CORTEX, a shipboard XRF-scanner for element analysis in split sediment cores, *Marine Geology, 151*, 143-153.

Keigwin, L., and Jones, G. (1994) Western North Atlantic evidence for millennial-scale changes in ocean circulation and climate. *Journal of Geophysical Research, 99,* 12397-12410.

Koltermann, K., Gouretski, V. and Jancke K. (eds.) (2011). In: Sparrow, M., Chapman, P. and Gould, J. (eds) *Hydrographic Atlas of the World Ocean Circulation Experiment (WOCE) Volume 3: Atlantic Ocean*. International WOCE Project Office, Southampton, UK, ISBN 090417557X.

Le, J. and Shackleton, N. (1992). Carbonate dissolution fluctuations in the Western Equatorial Pacific during the Late Quaternary. *Paleoceanography, 7,* 21-42.

Lisiecki, L. and Raymo, M. (2005). A Pliocene-Pleistocene stack of 57 globally distributed benthic d^{18}O records, *Paleoceanography, 20*, PA1003, doi:10.1029/2004PA001071.

Marchitto, T. and Broecker, W. (2006). Deep water mass geometry in the glacial Atlantic Ocean: A review of constraints from the paleonutrient proxy Cd/Ca, *Geochemistry Geophysics Geosystems, 7,* Q12003, 1-16.

Marson, J., Mysak, L., Mata, M., and Wainer, I. (2016). Evolution of the deep Atlantic water masses since the last glacial maximum based on a transient run of NCAR-CCSM3, *Climate Dynamics, 47*, 865-877.

Millero, F. (2007). The Marine Inorganic Carbon Cycle. *Chemical Review, 107*, 308-341.

Milliman, J. (1993). Production and Accumulation of Calcium Carbonate in the Ocean: Budget of a Nonsteady State. *Global Biogeochemical Cycles, 7*, 927-957.

Milliman, J. and Farnsworth, K. (eds.) (2013). *River Discharge to the Coastal Ocean: A Global Synthesis*. Cambridge, GB: Cambridge University Press, 2013.

Morse, J. and Mackenzie, F. (eds.) (1990). *Geochemistry of Sedimentary Carbonates. 48*, Elsevier; New York, NY.

Nelson, C., Hendy, C., Cuthbertson, A. and Jarrett, G. (1986). Late Quaternary carbonate and isotope stratigraphy, subantarctic Site 594, Southwest Pacific. In: Kennett, JP; von der Borch, CC; et al. (eds.), *Initial Reports of the Deep Sea Drilling Project, Washington (U.S. Govt. Printing Office)*, ***90***, 1425-1436.

Nelson, G., and Hutchings, L. (1983). The Benguela Upwelling Area, *Prog Oceanography, 12*, 333-356.

Neumann, A. (1965). Processes of recent carbonate sedimentation in Harrington Sound, Bermuda. *Bulletin of Marine Science, 15*, 987-1035.

Ostermann, D., and Curry, W. (2000). Calibration of stale isotopic data: An enriched $\delta^{18}O$ standard used for source gas mixing detection and correction, *Paleoceanography, 15*, 353-360.

Petit, J., Jouzel, J., Raynaud, D., Barkov, N., Barnola, J., Basile, I., Benders, M., Chappellaz, J., Davis, M., Delaygue, G., Delmotte, M., Kotlyakov, V., Legrand, M., Lipenkov, V., Lorius, C., Pepin, L., Ritz, C., Saltzman, E. and Stievenard, M. (1999). Climate and atmospheric history of the past 420,000 years from the Vostok ice core, Antarctica. *Nature, 399,* 429-436.

Piela, C. (2010). Equatorial Pacific Sediment Deposition during the Early to Middle Miocene: Carbon Cycling and Proxies for Productivity. Master's Thesis, Texas A&M University, College Station, Texas.

Pierrot, D., and Wallace, D. (2006). MS Excel Program Developed for CO2 System Calculations. ORNL/CDIAC-105a. Carbon Dioxide Information Analysis Center, Oak Ridge National Laboratory, U.S. Department of Energy, Oak Ridge, Tennessee. doi: 10.3334/CDIAC/otg.CO2SYS_XLS_CDIAC105a

Rea, D. (1994). The Paleoclimatic record provided by Eolian Deposition in the Deep Sea: The Geologic History of Wind, *Reviews of Geophysics, 32*, 159-195.

Reid, J. (1994). On the total geostrophic circulation of the North Atlantic Ocean: Flow patterns, tracers, and transports. *Progressive Oceanography, 33,* 1-92.

Reid, J. (1996). On the Circulation of the South Atlantic Ocean. In: Wefer, G., Berger, W., Siedler, Webb, G. (eds.), *The South Atlantic: Present and Past Circulation*. Springer-Verlag Berlin Heidelberg, 13-44.

Richter, T., Van der Gaast, S., Koster, B., Vaars, A., Gieles, R., de Stigter, H., De Haas, H. and van Weering T. (2006). The Avaatech XRF Core Scanner: technical description and application to NE Atlantic sediments, In: Rothwell, R.G. (ed.),

New Techniques in Sediment Core Analysis, Geological Society Special Publications, 267(1), 39-50, doi: 10.1144/GSL.SP.2006.267.01.03.

Schmaltz, J. (2015, May). *Dust Plumes off Namibia*. Retrieved from NASA Earth Observatory: http://eoimages.gsfc.nasa.gov/images/imagerecords/81000/81073/namibia_tmo_2013125_lrg.jpg

Shackleton, N. and Opdyke, N. (1972). Oxygen Isotope and Palaeomagnetic Stratigraphy of Equatorial Pacific Core V28-238: Oxygen Isotope Temperatures and Ice Volumes on a 10^5 Year and 10^6 Year Scale. *Quaternary Research, 3*, 39-55.

Shaffer, F. (1984). The Origin of the Walvis Ridge: Sediment/Basalt Compensation during Crustal Separation. *Paleogeography, Paleoclimatology, Paleoecology, 45*, 87-100.

Shannon, L. and Anderson, F. (1982). Applications of satellite ocean colour imagery in the study of the Benguela Current system. *South African Journal of Photogrammetry, Remote Sensing and Cartographgy, 13,* 153-169.

Shannon, L. (1985). The Benguela Ecosystem Part 1: Evolution of the Benguela, Physical Features and Processes. *Oceanography Marine Biology Annual Review, 23,* 105-182.

Slowey, N., and Curry, W. (1995). Glacial-interglacial differences in circulation and carbon cycling within the upper western North Atlantic, *Paleoceanography, 10,* 715-732.

Wefer, G. Berger, W., Siedler, G. and Webb, D. (eds.) (1996*). The South Atlantic: Present and Past Circulation.* Springer-Verlag Berlin Heidelberg, 363-410

Waelbroeck, C., Labeyrie, L., Michel, E., Duplessy, J., McManus, J., Lambeck., Balbon., Labracherie, M. (2002). Sea-level and deep water temperature changes derived from benthic foraminifera isotopic records. *Quaternary Science Reviews, 21,* 295-305.

Yu, J., Menviel, L., Jin, Z., Thornalley, D., Barker, S., Marino, G., Rohling, E., Cai, Y., Zhang, F., Wang, X., Dai, Y., Chen, P. and Broecker, W. (2016). Sequestration of carbon in the deep Atlantic during the last glaciation, *Nature Geoscience 9*, 319- 324.

Zahn, R., Sarnthein, M. and Erlenkeuser, H. (1987). Benthic isotope evidence for changes of the Mediterranean outflow during the late Quaternary. *Paleoceanography 2*, 543-559. doi:10.1029/PA002i006p00543

APPENDIX A

JPC21

Depth (m)	Age (ky)	%$CaCO_3$	Depth (m)	Age (ky)	%$CaCO_3$
0.03	2.59	79.58	5.20	126.27	79.07
0.20	7.58	83.76	5.40	128.56	76.87
0.40	10.02	81.28	5.60	137.40	71.93
0.60	12.28	78.50	5.80	157.40	72.67
0.80	14.54	75.12	6.00	N/A	77.15
1.00	16.80	67.94	6.20	N/A	70.81
1.20	20.66	61.77	6.40	N/A	69.37
1.40	25.89	65.92	6.60	N/A	66.57
1.60	31.11	69.85	6.80	N/A	72.09
1.80	36.33	71.49			
2.00	41.56	76.57			
2.20	46.78	68.45			
2.40	52.00	74.48			
2.60	57.22	66.94			
2.80	62.45	60.26			
3.00	67.62	68.13			
3.20	72.69	75.48			
3.40	77.76	74.17			
3.60	82.83	75.34			
3.80	86.46	80.06			
4.00	90.60	74.64			
4.20	95.75	76.79			
4.40	101.97	79.45			
4.60	108.19	78.35			
4.80	114.22	78.85			
5.00	120.22	81.67			

JPC13

Depth (m)	Age (ky)	%$CaCO_3$	Depth (m)	Age (ky)	%$CaCO_3$	Depth (m)	Age (ky)	%$CaCO_3$
0.01	3.11	80.78	3.41	49.10	73.09	7.01	114.64	79.61
0.11	5.53	84.10	3.51	50.66	74.54	7.11	117.92	82.79
0.21	8.33	83.37	3.61	52.22	73.32	7.21	121.24	82.14
0.31	10.39	80.54	3.71	53.78	76.02	7.31	123.60	80.44
0.41	11.93	81.55	3.81	55.34	73.49	7.41	125.68	75.26
0.51	13.48	79.96	3.87	56.27	71.99	7.51	127.76	70.31
0.61	15.03	77.76	3.97	58.05	66.58	7.60	129.64	65.56
0.71	16.58	76.41	4.07	59.39	67.78	7.70	131.72	70.36
0.78	17.16	76.38	4.37	63.26	54.79	7.80	133.80	68.97
0.88	17.79	73.14	4.47	64.60	58.84	7.90	135.88	70.93
0.98	18.42	70.22	4.57	65.89	63.64	8.00	137.96	74.66
1.08	19.06	66.16	4.67	67.17	67.56	8.10	140.04	75.33
1.18	20.05	60.70	4.77	68.45	74.49	8.20	142.12	72.31
1.28	21.10	60.73	4.87	70.07	76.07	8.30	144.20	70.06
1.38	22.15	57.84	4.97	71.81	76.06	8.31	144.51	74.55
1.48	23.19	59.36	5.07	73.54	77.35	8.41	146.59	71.39
1.58	24.24	59.96	5.17	75.28	76.21	8.51	148.67	64.61
1.61	24.55	58.85	5.30	78.00	74.30	8.61	150.75	64.19
1.71	25.60	58.68	5.40	79.64	74.63	8.71	152.84	67.19
1.81	26.75	63.43	5.50	80.91	74.63	8.81	154.92	61.47
1.91	27.92	64.38	5.70	83.44	78.93	8.91	157.00	63.33
2.01	29.08	67.11	5.80	85.32	77.38	9.01	159.08	56.07
2.11	30.24	62.85	5.90	87.68	80.86	9.10	160.95	61.33
2.21	31.40	64.31	6.00	90.21	76.23	9.13	161.47	76.72
2.41	33.80	68.32	6.10	92.78	76.78	9.23	163.55	63.71
2.51	35.32	74.89	6.20	95.35	75.84	9.33	165.63	60.79
2.61	36.84	74.34	6.30	97.92	77.91	9.43	167.71	52.84
2.71	38.36	73.31	6.40	100.49	77.29	9.53	169.79	70.35
2.81	39.88	74.09	6.50	103.07	78.86	9.63	171.87	70.67
2.91	41.39	75.14	6.60	105.64	80.01	9.73	173.95	76.27
3.01	42.91	77.20	6.70	107.98	78.88	9.83	176.03	75.40
3.11	44.43	75.85	6.80	110.13	78.08	9.83	176.14	75.53
3.21	45.97	71.36	6.81	110.35	79.14	9.93	178.22	77.95
3.31	47.54	74.79	6.91	112.49	81.28	10.03	180.30	80.20

JPC13 cont.		
Depth (m)	**Age (ky)**	**%$CaCO_3$**
10.13	182.38	81.32
10.23	184.46	80.89
10.33	186.54	76.54
10.43	188.62	75.39
10.53	190.70	58.71
10.63	192.78	63.28
10.73	194.86	72.34
10.83	196.95	78.03

JPC15

Depth (m)	Age (ky)	%$CaCO_3$	Depth (m)	Age (ky)	%$CaCO_3$	Depth (m)	Age (ky)	%$CaCO_3$
0.05	2.90	82.73	1.96	33.19	63.29	3.76	57.17	69.44
0.15	5.34	84.31	2.01	33.71	62.20	3.81	58.02	69.87
0.16	5.58	84.43	2.06	34.16	60.94	3.87	59.02	72.91
0.25	7.34	83.17	2.11	34.62	62.27	3.92	59.59	72.97
0.35	9.20	82.97	2.36	37.40	65.73	3.97	60.13	73.83
0.45	11.05	81.68	2.41	38.17	62.64	4.02	60.66	74.47
0.55	12.91	80.19	2.46	38.91	60.95	4.07	61.20	70.90
0.64	14.58	75.87	2.51	39.65	63.65	4.12	61.73	71.48
0.71	15.88	73.95	2.56	40.40	66.80	4.17	62.47	72.39
0.79	17.05	75.24	2.61	41.14	68.91	4.22	63.26	74.80
0.85	17.53	74.16	2.66	41.88	69.54	4.27	64.05	73.19
0.90	17.93	66.22	2.71	42.62	68.64	4.32	64.84	71.93
0.95	18.33	63.90	2.76	43.20	66.57	4.37	65.63	70.33
1.00	18.74	61.90	2.81	43.72	67.09	4.42	66.42	69.35
1.05	19.17	61.77	2.86	44.25	70.40	4.47	67.21	67.18
1.10	19.65	58.55	2.91	44.77	72.97	4.52	68.00	66.55
1.15	20.15	58.03	2.96	45.39	74.15	4.57	68.79	65.14
1.20	20.66	57.65	3.01	46.07	72.63	4.62	69.91	58.02
1.25	21.16	58.43	3.06	46.76	72.47	4.67	71.02	57.16
1.30	21.67	57.63	3.11	47.44	71.53	4.73	72.36	56.92
1.35	22.42	57.31	3.16	48.13	71.95	4.78	73.48	56.26
1.40	23.20	60.50	3.21	48.81	74.46	4.83	74.60	54.96
1.45	23.98	56.71	3.26	49.53	77.15	4.88	75.76	55.19
1.51	24.91	60.50	3.31	50.26	77.25	4.93	77.03	58.07
1.55	25.54	60.47	3.36	50.99	75.15	4.98	78.30	58.05
1.61	26.47	59.49	3.41	51.72	76.27	5.03	79.56	64.92
1.66	27.25	56.68	3.46	52.46	77.52	5.08	80.83	62.68
1.71	28.03	58.32	3.51	53.19	75.02	5.13	82.10	67.35
1.76	28.81	58.82	3.56	53.92	72.91	5.18	83.37	75.67
1.81	29.59	58.75	3.61	54.65	72.10	5.23	84.82	70.21
1.86	30.37	61.92	3.66	55.49	71.03	5.28	86.46	73.48
1.91	31.64	63.16	3.71	56.33	68.52	5.33	88.10	74.47

JPC15 cont.

Depth (m)	Age (ky)	%$CaCO_3$	Depth (m)	Age (ky)	%$CaCO_3$
5.38	89.74	75.25	8.72	162.54	62.36
5.40	90.40	77.81	8.82	164.33	70.05
5.50	93.68	74.26	8.92	166.14	63.60
5.60	96.97	73.48	9.02	167.94	61.23
5.70	100.25	75.70	9.12	169.70	58.54
5.80	103.53	77.06	9.22	171.85	55.06
5.90	106.81	80.54	9.32	174.41	62.23
6.00	110.10	76.64	9.42	176.98	57.51
6.10	113.38	75.52	9.52	179.55	54.76
6.20	117.10	75.81	9.62	182.11	51.45
6.30	121.05	76.89	9.72	184.68	71.52
6.40	123.80	79.21	9.82	187.25	71.23
6.50	125.57	76.96			
6.60	127.33	77.54			
6.70	129.09	79.73			
6.80	130.72	79.01			
6.90	132.24	82.37			
7.00	133.76	82.00			
7.10	135.28	77.43			
7.20	136.80	76.97			
7.30	138.27	69.28			
7.40	139.65	72.10			
7.50	141.02	72.28			
7.60	142.39	69.46			
7.70	143.76	70.20			
7.80	145.14	75.49			
7.90	146.63	71.87			
8.00	148.84	76.23			
8.10	151.04	75.55			
8.20	153.24	69.38			
8.30	155.13	70.48			
8.40	156.92	72.77			
8.42	157.18	71.78			
8.52	158.97	69.16			
8.62	160.75	64.71			

JPC19

Depth (m)	Age (ky)	%$CaCO_3$	Depth (m)	Age (ky)	%$CaCO_3$	Depth (m)	Age (ky)	%$CaCO_3$
0.005	5.4393	77.91	3.17	66.25	73.52	6.33	143.27	75.08
0.11	7.77	74.42	3.27	66.80	74.97	6.43	144.73	71.84
0.21	8.67	79.56	3.30	69.19	76.55	6.53	146.15	68.26
0.29	9.83	84.47	3.40	73.19	75.15	6.63	148.20	72.85
0.39	11.14	81.66	3.50	76.10	74.79	6.73	150.32	70.37
0.49	12.42	80.59	3.60	78.35	76.16	6.83	152.42	65.90
0.59	13.64	78.50	3.695	82.233	77.34	6.93	154.56	62.10
0.69	15.15	79.29	3.80	85.35	76.96	7.03	156.97	62.25
0.79	17.58	72.68	3.90	90.31	78.30	7.13	N/A	64.00
0.89	18.67	75.05	4.10	91.76	71.99	7.23	N/A	61.96
0.99	19.25	67.45	4.20	94.64	75.60			
1.09	20.38	60.55	4.30	97.53	77.67			
1.19	21.58	60.72	4.40	100.67	73.74			
1.29	22.89	58.13	4.50	103.92	73.34			
1.39	24.20	56.84	4.60	107.17	78.45			
1.49	25.51	60.43	4.70	110.91	76.78			
1.59	26.82	58.71	4.81	114.16	74.03			
1.69	28.27	64.28	4.91	117.41	71.03			
1.77	30.48	75.66	5.01	120.67	69.67			
1.87	32.55	69.98	5.11	123.08	69.81			
1.97	35.12	71.91	5.21	124.91	69.87			
2.07	37.68	70.29	5.31	126.74	67.30			
2.17	40.24	70.54	5.41	128.57	69.36			
2.27	42.81	69.83	5.51	130.30	72.99			
2.37	44.89	65.47	5.61	131.82	74.34			
2.47	46.92	55.99	5.71	133.34	76.37			
2.57	51.56	58.68	5.81	134.85	76.96			
2.67	55.49	57.75	5.91	136.37	79.16			
2.77	57.59	63.91	6.01	137.98	80.02			
2.87	59.50	68.66	6.11	139.77	83.75			
2.97	62.31	65.62	6.21	141.48	77.83			
3.07	64.05	71.36	6.31	141.78	74.05			

JPC23

Depth (m)	Age (ky)	%$CaCO_3$	Depth (m)	Age (ky)	%$CaCO_3$	Depth (m)	Age (ky)	%$CaCO_3$
0.03	6.39	79.03	3.17	78.34	62.89	6.925	141.57	68.11
0.12	7.66	80.2	3.27	79.79	63.26	7.025	142.99	67.52
0.22	9.07	81.635	3.37	81.16	63.47	7.125	144.41	57.61
0.32	10.48	79.55	3.47	82.38	63.745	7.225	145.84	56.34
0.42	11.90	80.12	3.57	83.60	68.28	7.36	147.75	58.47
0.52	13.31	73.8	3.67	84.98	76.37	7.46	149.17	56.84
0.62	14.59	71.61	3.765	86.445	74.32	7.56	150.6	57.89
0.72	15.75	71.98	3.865	87.909	74.27	7.66	152.02	53.61
0.82	16.92	74	3.965	89.374	65.78	7.79	153.86	47.98
0.92	18.09	70.11	4.065	90.838	64.5	7.85	154.72	49.12
1.02	19.31	63.92	4.165	92.302	65.15	7.96	156.28	46.22
1.13	21.67	64.04	4.265	93.766	66.91	8.06	157.7	62.54
1.22	24.11	63.27	4.365	95.23	70.82	8.16	159.12	64.48
1.32	27.74	66.82	4.465	96.694	73.56	8.26	160.54	71.1
1.42	31.43	67.96	4.565	98.159	71.59	8.36	161.96	71.09
1.52	35.04	62.62	4.665	99.659	71.29	8.46	163.38	70.55
1.62	37.58	72.3	4.765	102.09	75.2	8.55	164.66	72.84
1.72	39.99	68.41	4.905	105.59	68.96	8.58	165.09	70.2
1.82	42.39	71.39	5.005	109.03	72.21	8.68	166.51	69.4
1.92	44.80	70.735	5.105	112.02	72.92	8.78	167.93	70.96
2.02	47.20	71.65	5.205	114.16	76.55	8.88	169.35	75.25
2.12	49.77	69.22	5.305	116.68	74.99	8.98	170.77	76.075
2.23	52.64	70.4	5.405	119.2	76.36	9.08	172.19	73.86
2.32	54.98	65.975	5.505	121.4	79.34			
2.39	56.80	67.48	5.595	122.68	79.93			
2.47	58.89	67.41	5.695	124.1	76.49			
2.57	61.49	62.04	5.795	125.52	72.52			
2.67	64.22	61.96	5.895	126.94	70.51			
2.77	67.30	64.41	5.995	128.36	74.16			
2.87	70.06	64.74	6.075	129.5	71.265			
2.97	72.82	71.75	6.125	130.21	73.05			
3.07	75.58	70.045	6.225	131.63	69.77			

JPC27 and GC26

Depth (m)	Age (ky)	%$CaCO_3$	Depth (m)	Age (ky)	%$CaCO_3$
0.03	3.75	76.99	5.90	136.16	72.82
0.11	7.78	78.17	6.10	142.40	70.195
0.13	8.18	76.98	6.30	148.64	71.47
0.30	10.55	76.985	6.50	154.89	73.7
0.50	13.04	75.74	6.70	161.13	76.84
0.70	15.84	68.26	6.90	167.37	71.34
0.90	19.74	67.36	7.1	173.62	68.02
1.10	23.99	61.41	7.3	179.86	68.65
1.30	28.24	57.9	7.5	186.1	61.5
1.50	40.70	64.06	7.7	192.34	63.84
1.62	42.45	69.07	7.9	198.59	56.62
1.70	43.60	65.315	8.1	204.83	54.8
1.90	46.48	69.95	8.3	211.07	46.83
2.10	51.45	63.23	8.5	217.32	43.58
2.30	55.56	62.28	8.7	N/A	62.565
2.50	59.43	65.8	8.9	N/A	67.38
2.70	63.41	59.54	9.1	N/A	69.5
2.90	70.30	55.29	9.3	N/A	67.42
3.10	74.14	64.73	9.5	N/A	74.2
3.30	77.97	67.93			
3.50	81.57	62.415			
3.70	84.24	69.97			
3.90	86.18	74.3			
4.10	88.11	67.75			
4.30	92.94	64.5			
4.50	95.92	68.32			
4.70	102.29	72.43			
4.90	108.48	71.63			
5.10	112.96	70.95			
5.30	117.44	71.325			
5.50	121.93	74.34			
5.70	129.92	78.98			

JPC48

Depth (m)	Age (ky)	%$CaCO_3$	Depth (m)	Age (ky)	%$CaCO_3$	Depth (m)	Age (ky)	%$CaCO_3$
0.01	N/A	82.67	3.32	68.65	71.76	6.28	134.3	79.83
0.11	3.79	85.49	3.42	70.59	79.01	6.38	139.18	79.72
0.21	4.81	86.97	3.52	72.50	77.78	6.48	143.58	75.04
0.31	5.83	86.835	3.62	74.41	80.26			
0.41	6.85	88.07	3.72	78.74	83.69			
0.51	10.42	85.99	3.7	78.29	81.04			
0.71	16.08	76.9	3.74	79.094	80.94			
0.81	17.66	71.69	3.84	80.434	80.445			
0.91	19.23	68.35	3.94	81.799	80.47			
1.01	20.74	65.31	4.04	83.175	81.27			
1.11	22.25	67.52	4.14	84.715	80.46			
1.21	23.90	65.545	4.24	87.727	80.115			
1.29	25.26	75.45	4.34	90.739	83.46			
1.39	26.95	72.255	4.44	92.977	82.32			
1.49	28.64	72.92	4.54	94.883	81.5			
1.59	30.34	77.84	4.64	96.789	82			
1.69	32.03	79.84	4.74	98.696	78.01			
1.79	36.96	80.9	4.84	100.6	83.42			
1.89	39.51	79.71	4.94	102.51	83.74			
1.99	42.06	79.87	4.97	103.08	84.36			
2.09	44.61	81.35	5.07	104.99	83.415			
2.19	47.04	78.36	5.17	106.89	84.4			
2.29	49.33	82.02	5.27	108.8	82.29			
2.39	51.63	80.42	5.37	111.79	83.12			
2.49	53.92	79.65	5.47	115.38	84.06			
2.62	56.91	78.935	5.57	117.6	84.42			
2.72	58.35	78.56	5.67	119.31	83.83			
2.82	59.75	76.55	5.77	121.03	83.77			
2.92	61.16	76.02	5.97	124.46	84.815			
3.02	62.48	66.315	6.07	125.85	83.2			
3.12	63.76	69.31	6.17	127.01	81.29			
3.22	65.43	64.6	6.18	127.12	82.04			

JPC49

Depth (m)	Age (ky)	%$CaCO_3$	Depth (m)	Age (ky)	%$CaCO_3$
0.2	5.70	86.04	6.6	161.99	77.74
0.4	10.19	81.79	6.8	172.31	78.51
0.6	15.25	81.77	7	182.62	68.63
0.8	18.51	68.72	7.2	192.94	69.3
1	21.11	64.52	7.4	203.25	61.98
1.2	26.28	67.89	7.6	213.57	83.23
1.4	32.39	72.025	7.8	223.89	85.49
1.6	36.41	81.64	8	234.2	82.34
1.8	41.31	79.31	8.2	244.52	72.7
2	46.21	83.03	8.4	254.83	84.42
2.2	51.11	79.925	8.6	265.15	75.37
2.4	56.01	78.62	8.8	275.46	79.935
2.6	60.03	73.29	9	285.78	77.73
2.8	63.91	66.445	9.2	296.1	62.31
3	67.97	75.78			
3.2	71.28	76.41			
3.4	74.40	82.12			
3.6	79.80	80.3			
3.8	83.57	82.02			
4	87.64	80.77			
4.2	91.75	84.43			
4.4	95.85	81.95			
4.6	99.96	82.955			
4.8	104.07	84.06			
5	108.29	84.08			
5.2	113.01	85.33			
5.4	118.04	84.005			
5.6	122.70	85.24			
5.8	126.75	83.21			
6	131.04	78.89			
6.2	141.36	80.68			
6.4	151.67	76.03			

JPC64

Depth (m)	Age (ky)	%$CaCO_3$	Depth (m)	Age (ky)	%$CaCO_3$	Depth (m)	Age (ky)	%$CaCO_3$
0.03	N/A	79.56	3.32	54.09	59.24	7.11	151.53	62.69
0.11	N/A	81.79	3.42	58.75	52.82	7.21	155.21	56.99
0.21	7.55	81.42	3.52	60.93	43.58	7.31	158.9	58.64
0.31	9.82	81.90	3.62	62.23	42.05	7.41	162.58	61.655
0.41	11.00	81.64	3.77	64.20	40.32	7.6	169.58	63.775
0.51	12.18	79.21	3.87	65.54	46.86	7.8	176.96	54.03
0.61	13.38	78.29	3.97	66.887	48	8	184.33	70.71
0.71	14.57	74.92	4.07	68.23	49.725			
0.81	15.77	69.67	4.17	69.603	62.24			
0.91	16.90	67.04	4.27	70.994	66.5			
1.01	17.39	55.25	4.37	72.386	68.04			
1.11	17.88	53.07	4.47	73.778	70.38			
1.30	18.80	46.93	4.57	75.17	66.46			
1.40	19.25	45.17	4.67	76.562	67.9			
1.50	19.80	46.23	4.77	77.953	64.95			
1.60	20.92	46.72	4.87	80.141	62.23			
1.70	23.57	46.49	4.97	84.187	62.88			
1.80	24.84	52.39	4.99	84.887	62.07			
1.90	26.10	48.34	5.09	88.389	66.08			
2.00	27.36	47.57	5.19	92.159	63.17			
2.10	28.63	49.52	5.29	95.45	65.265			
2.20	29.90	60.58	5.39	98.309	69.78			
2.30	31.32	56.49	5.49	101.17	69.92			
2.40	32.74	55.24	5.59	104.03	67.46			
2.52	34.44	55.21	5.69	106.89	68.195			
2.62	36.10	59.54	5.79	109.74	67.95			
2.72	39.18	55.58	5.89	113.09	74.14			
2.82	42.26	56.17	5.99	116.6	76.14			
2.92	45.13	60.52	6.09	120.12	78.245			
3.02	46.87	60.27	6.21	124.18	78.715			
3.12	48.60	60.57	6.31	125.44	77.12			
3.22	50.34	59.53	6.41	126.69	72.23			

JPC66

Depth (m)	Age (ky)	%$CaCO_3$	Depth (m)	Age (ky)	%$CaCO_3$	Depth (m)	Age (ky)	%$CaCO_3$
0.01	N/A	59.64	3.20	47.84	60.08	6.29	113.45	76.19
0.11	4.68	79.07	3.30	51.17	57.19	6.39	115.81	58.44
0.19	6.07	79.08	3.40	53.80	57.54	6.49	118.17	79.19
0.23	6.77	80.37	3.50	57.87	52.71	6.59	120.53	68.5
0.33	8.51	73.42	3.60	60.59	51.96	6.69	122.88	77.97
0.43	10.25	79.52	3.70	61.96	44.56			
0.53	11.99	79.12	3.82	63.59	40.71			
0.63	13.73	75.35	3.92	65.32	42.175			
0.73	15.47	71.82	4.02	66.99	45.49			
0.83	16.59	74.10	4.12	67.70	47.73			
0.93	16.96	65.58	4.22	68.41	60.65			
1.03	17.32	60.22	4.32	69.14	61.27			
1.23	18.27	49.26	4.42	70.56	68.1			
1.33	19.56	47.63	4.52	72.00	66.76			
1.43	20.85	44.56	4.62	73.53	68.61			
1.53	22.14	41.64	4.72	75.21	50.78			
1.63	23.43	47.90	4.82	76.89	51.18			
1.73	24.75	45.67	4.92	78.57	60.97			
1.83	26.11	43.48	4.96	79.24	62.08			
1.93	27.70	45.96	5.06	82.06	59.92			
2.03	29.51	51.57	5.16	84.93	61.72			
2.13	31.27	56.39	5.26	87.80	64.78			
2.23	32.98	51.69	5.36	90.46	60.97			
2.33	34.81	52.13	5.46	92.94	63.11			
2.43	37.82	48.79	5.56	95.43	68.09			
2.53	39.67	51.17	5.66	97.92	68.57			
2.60	40.56	56.05	5.76	100.41	66.01			
2.70	41.93	44.70	5.86	102.89	65.05			
2.80	43.11	51.88	5.96	105.38	64.95			
2.90	44.19	51.79	6.06	107.87	67.04			
3.00	45.27	56.21	6.16	110.36	66.22			
3.10	46.31	57.95	6.19	111.09	72.255			

JPC68

Depth (m)	Age (ky)	%$CaCO_3$	Depth (m)	Age (ky)	%$CaCO_3$	Depth (m)	Age (ky)	%$CaCO_3$
0.01	N/A	76.25	3.18	42.03	49.06	6.325	86.672	63.51
0.11	6.84	76.96	3.28	43.90	49.47	6.425	89.61	56.17
0.21	8.03	79.64	3.38	45.71	54.50	6.525	92.569	54.09
0.31	9.22	81.25	3.48	47.34	56.59	6.625	95.423	57.28
0.41	11.65	79.65	3.58	48.96	55.69	6.755	98.229	65.23
0.52	14.45	77.48	3.68	50.67	54.68	6.855	101.6	65.44
0.62	15.11	73.91	3.775	53.038	54.02	6.955	104.46	61.035
0.72	15.77	66.81	3.875	55.409	54.68	7.055	107.31	62.35
0.82	16.43	71.73	3.975	57.779	52.62	7.155	110.17	60.5
0.92	17.09	59.32	4.075	60.06	51.76	7.255	N/A	60.99
1.02	17.75	54.39	4.18	61.604	45.68			
1.12	18.32	48.02	4.28	62.867	41.15			
1.22	18.84	43.14	4.38	63.745	37.755			
1.32	19.37	43.01	4.48	64.347	38.61			
1.42	20.30	42.04	4.58	64.875	41.38			
1.52	22.19	38.21	4.68	66.015	44.62			
1.62	23.70	43.60	4.78	67.145	43.57			
1.72	24.59	46.47	4.88	68.264	51.73			
1.77	25.78	45.79	4.98	69.232	56.98			
1.87	27.14	42.89	5.08	70.075	55.6			
1.97	28.00	44.18	5.18	70.919	61.595			
2.07	28.87	44.25	5.28	71.762	62.47			
2.17	29.74	51.52	5.38	72.606	66.65			
2.27	30.62	52.77	5.425	72.997	65.98			
2.37	31.50	54.28	5.525	74.08	66.275			
2.47	32.38	48.23	5.625	75.243	62.72			
2.57	33.26	49.12	5.725	76.652	61.38			
2.67	34.14	48.75	5.825	78.06	60.64			
2.77	35.02	41.53	5.925	79.468	57.875			
2.87	36.20	50.54	6.025	80.876	56.99			
2.98	38.27	47.40	6.125	81.7	58.88			
3.08	40.15	50.73	6.225	83.734	53.15			

JPC89								
Depth (m)	**Age (ky)**	**%$CaCO_3$**	**Depth (m)**	**Age (ky)**	**%$CaCO_3$**	**Depth (m)**	**Age (ky)**	**%$CaCO_3$**
0.11	N/A	47.23	3.28	8.40	40.22	6.40	13.89	21.55
0.21	2.99	49.65	3.38	8.58	41.52	6.50	14.06	25.61
0.31	3.17	49.18	3.48	8.75	38.84	6.60	14.24	27.90
0.41	3.35	49.40	3.58	8.93	36.20	6.70	14.42	30.51
0.51	3.52	54.14	3.68	9.11	34.82	6.80	14.59	31.98
0.61	3.70	54.62	3.78	9.28	32.78	6.90	14.77	34.74
0.71	3.87	53.91	3.89	9.47	28.64	7.00	14.94	33.19
0.81	4.05	52.74	3.98	9.63	30.76	7.10	15.13	34.96
0.91	4.23	50.06	4.08	9.81	35.62	7.20	15.32	33.12
1.01	4.40	48.81	4.18	9.98	34.12	7.30	15.50	32.77
1.11	4.58	48.13	4.28	10.16	31.82	7.40	15.69	31.85
1.21	4.75	44.51	4.38	10.34	31.42	7.55	15.96	30.01
1.31	4.93	42.54	4.48	10.51	N/A	7.6	16.1	30.7
1.41	5.11	44.31	4.58	10.69	32.10	7.7	16.3	27.8
1.46	5.20	48.10	4.68	10.86	34.88	7.8	16.5	25.6
1.56	5.38	40.82	4.78	11.04	35.92	7.9	16.7	27.5
1.66	5.55	39.04	4.88	11.22	37.18	8.0	17.0	27.8
1.76	5.73	36.87	4.98	11.39	38.02	8.1	17.5	22.1
1.86	5.91	35.22	5.08	11.57	37.53	8.2	17.9	19.7
1.96	6.08	32.86	5.17	11.73	31.39	8.3	18.1	21.2
2.06	6.26	38.71	5.27	11.90	36.07	8.4	18.3	26.6
2.16	6.43	36.04	5.37	12.08	32.58	8.5	18.5	25.9
2.26	6.61	33.59	5.47	12.25	31.31	8.6	18.6	27.4
2.36	6.78	37.31	5.57	12.43	30.75	8.7	18.8	26.8
2.46	6.96	37.09	5.67	12.61	36.07	8.8	19.0	24.9
2.56	7.14	37.48	5.77	12.78	39.45	8.9	19.1	25.9
2.68	7.35	38.22	5.87	12.96	39.03	9.0	19.3	27.8
2.78	7.52	37.12	5.97	13.13	35.73	9.1	19.5	28.2
2.88	7.70	41.68	6.07	13.31	37.05	9.2	19.6	22.8
2.98	7.87	45.67	6.17	13.48	32.65	9.3	19.8	21.6
3.08	8.05	41.05	6.27	13.66	28.64	9.4	20.0	18.7
3.18	8.23	43.46	6.31	13.73	26.95	9.5	21.5	22.3

JPC89 cont.

Depth (m)	Age (ky)	%$CaCO_3$
9.6	23.2	23.6
9.7	24.9	22.2
9.8	26.6	21.9
10.0	28.6	29.6
10.1	29.6	24.3
10.2	30.4	26.3
10.3	31.2	31.0
10.4	32.1	35.8
10.5	N/A	35.2
10.6	N/A	33.9
10.7	N/A	37.4